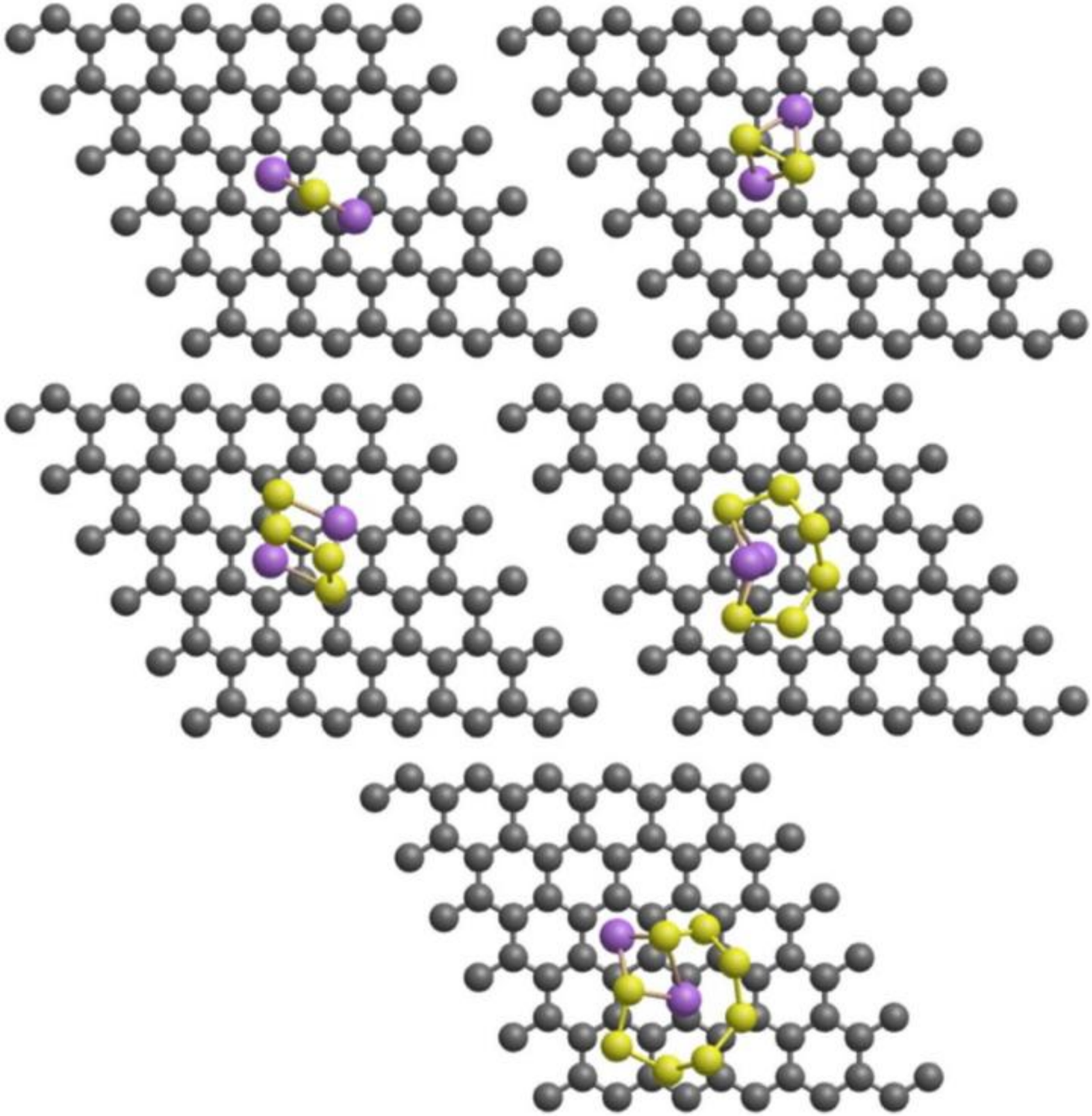

Figure 16. Illustration of atomic configurations for various LiPS species (Li_2S_x, $x = 1, 2, 4, 6, 8$) on a pristine graphene sheet. Grey, yellow and purple spheres represent C, S and Li atoms, respectively.

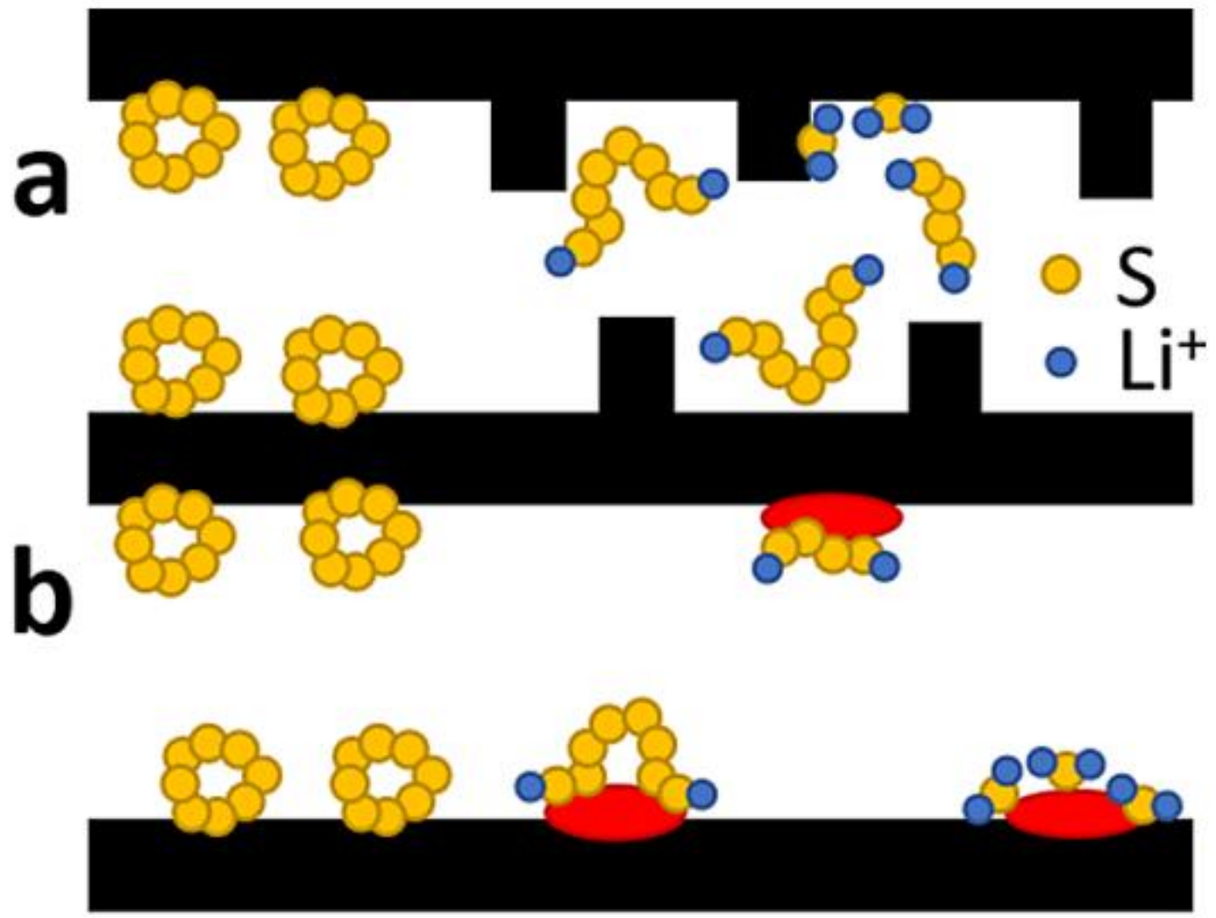

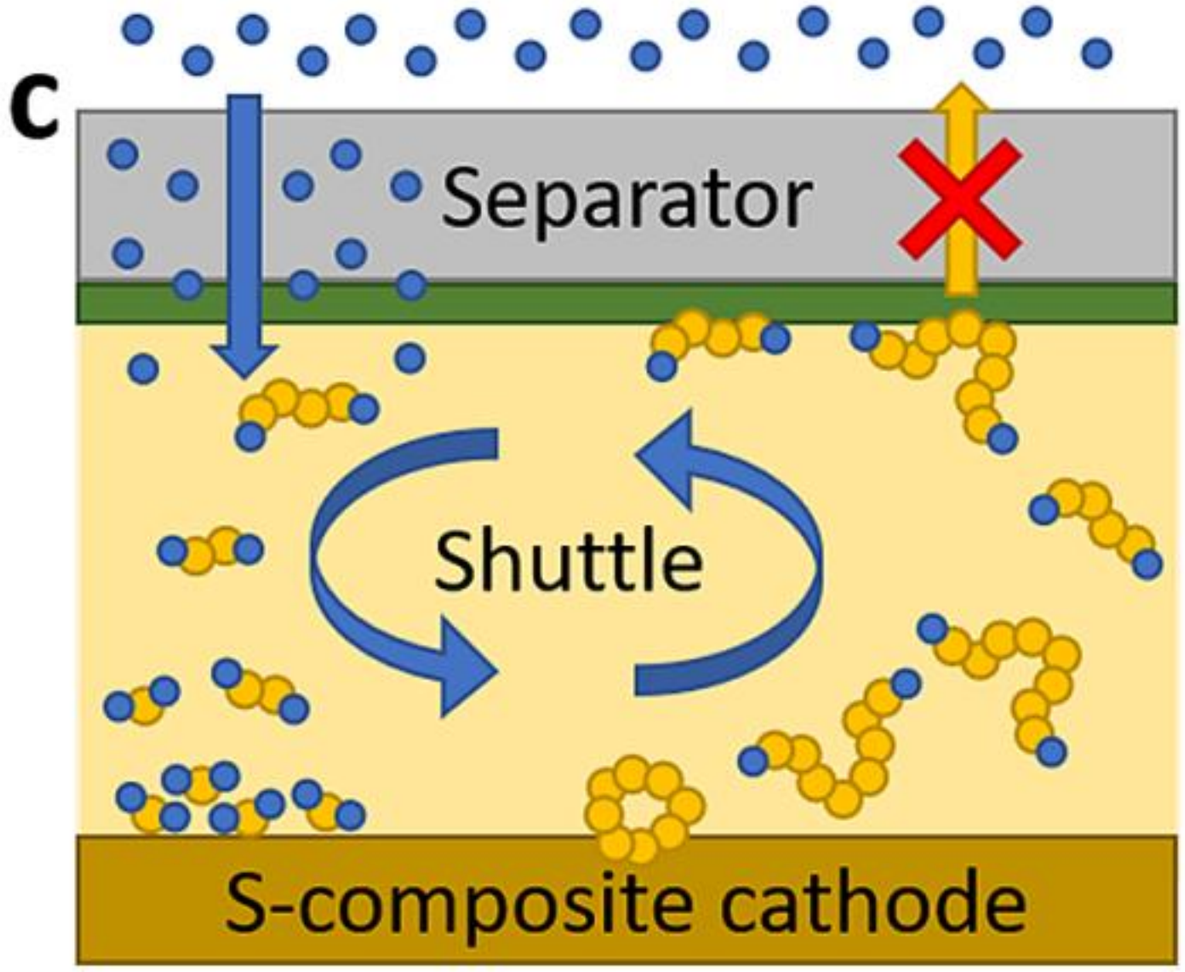

Figure 12. Schematics demonstrating the strategies employed to confine LiPSs. Within the cathode, LiPSs are prevented from diffusing into the bulk electrolyte by tortuous carbon matrices with long diffusion pathways (a), or by the adsorption of LiPSs onto chemical additives (red particles) doped on the C surface (b). (c) Interlayers (green section on separator) use chemical additives to adsorb LiPSs onto their surfaces, restricting the shuttle effect to the cathodic side of the battery, whilst maintaining

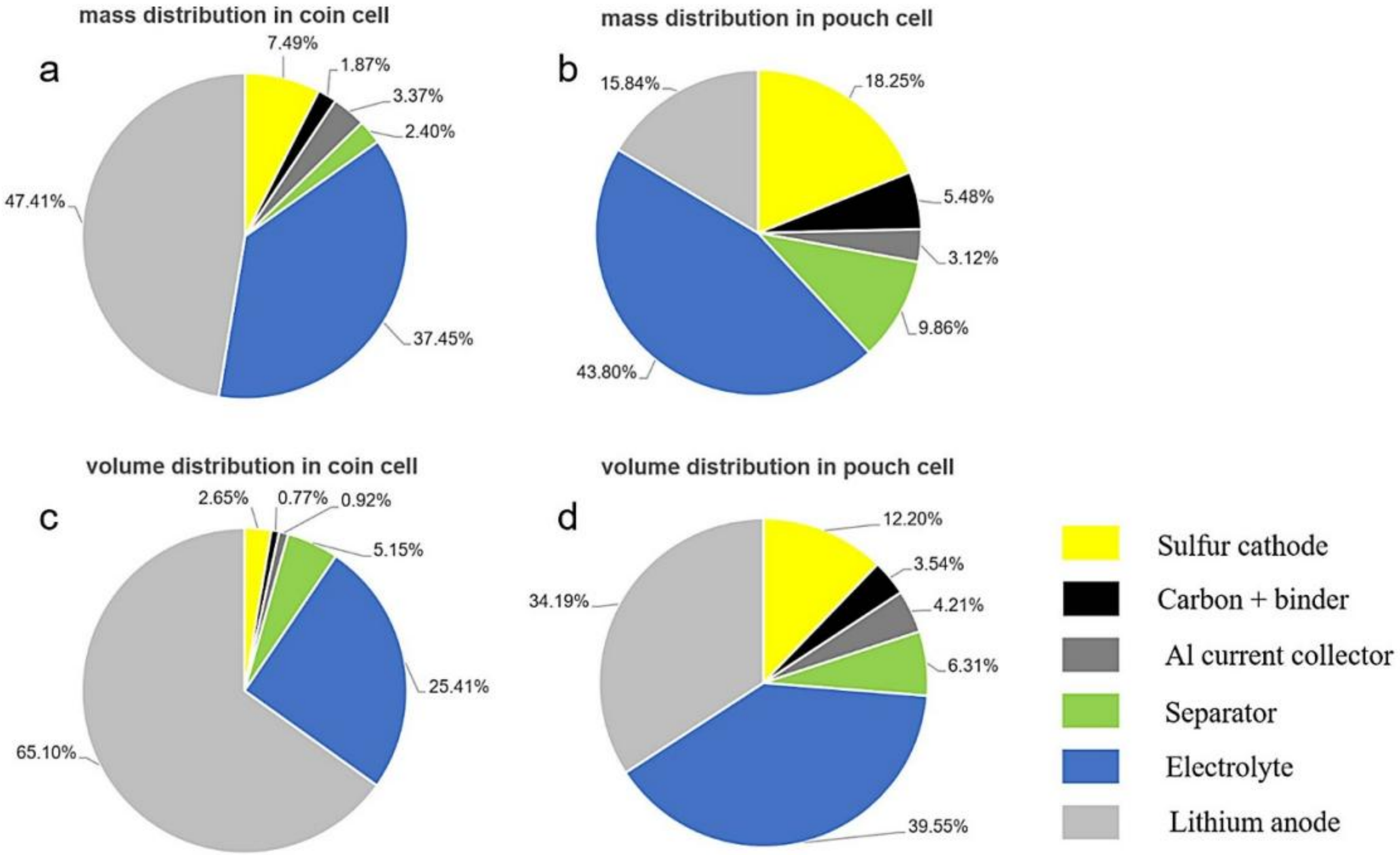

Figure 1. Mass distribution in (a) coin and (b) pouch cells. Volume distribution in (c) coin and (d) pouch cells. Calculation parameters for pouch cells: S content = 80%; S loading = 6 mg cm^{-2}; E/S = 2 μl mg^{-1}; N/P = 2; PP separator

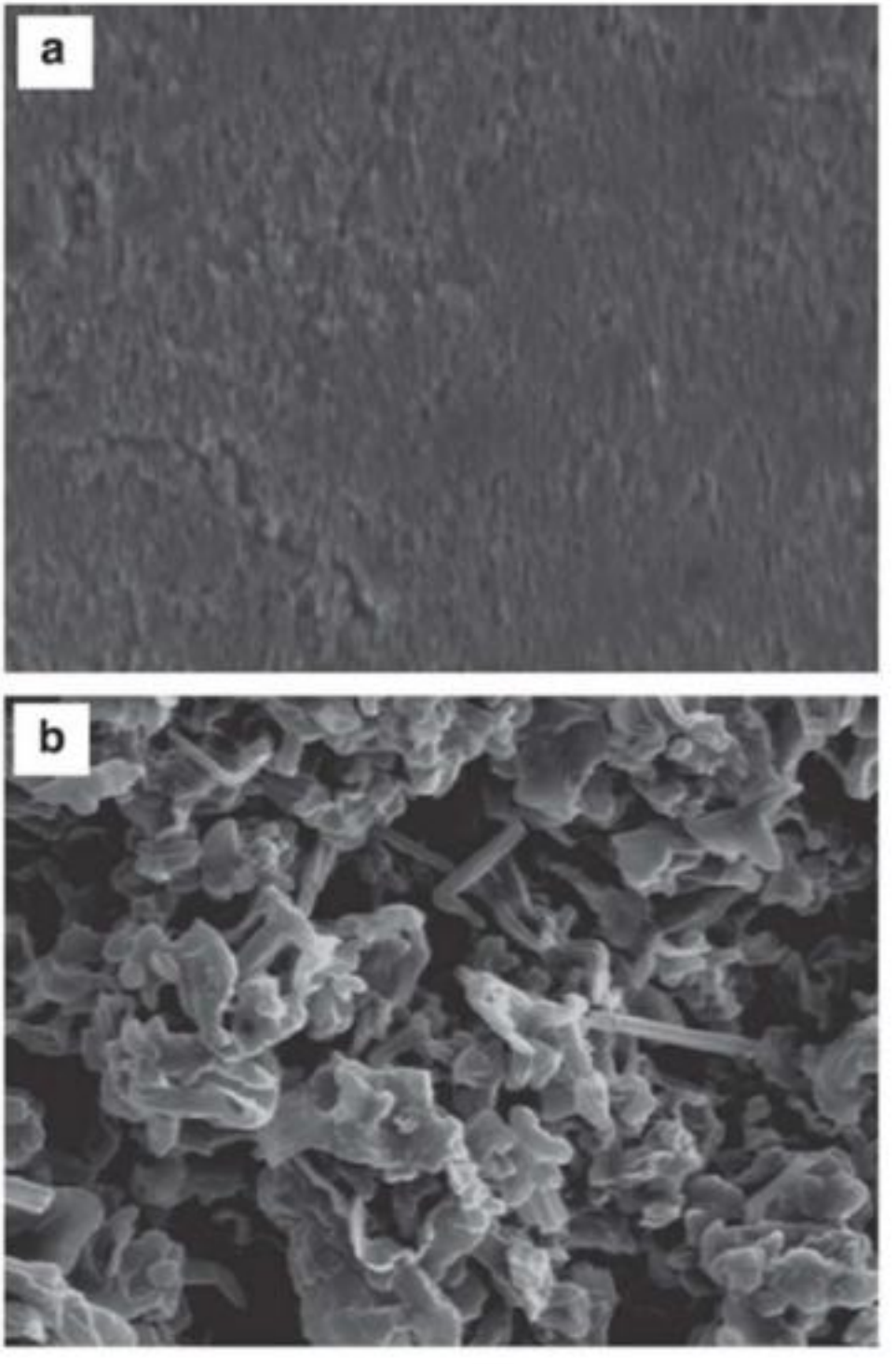
a
b
10 μm

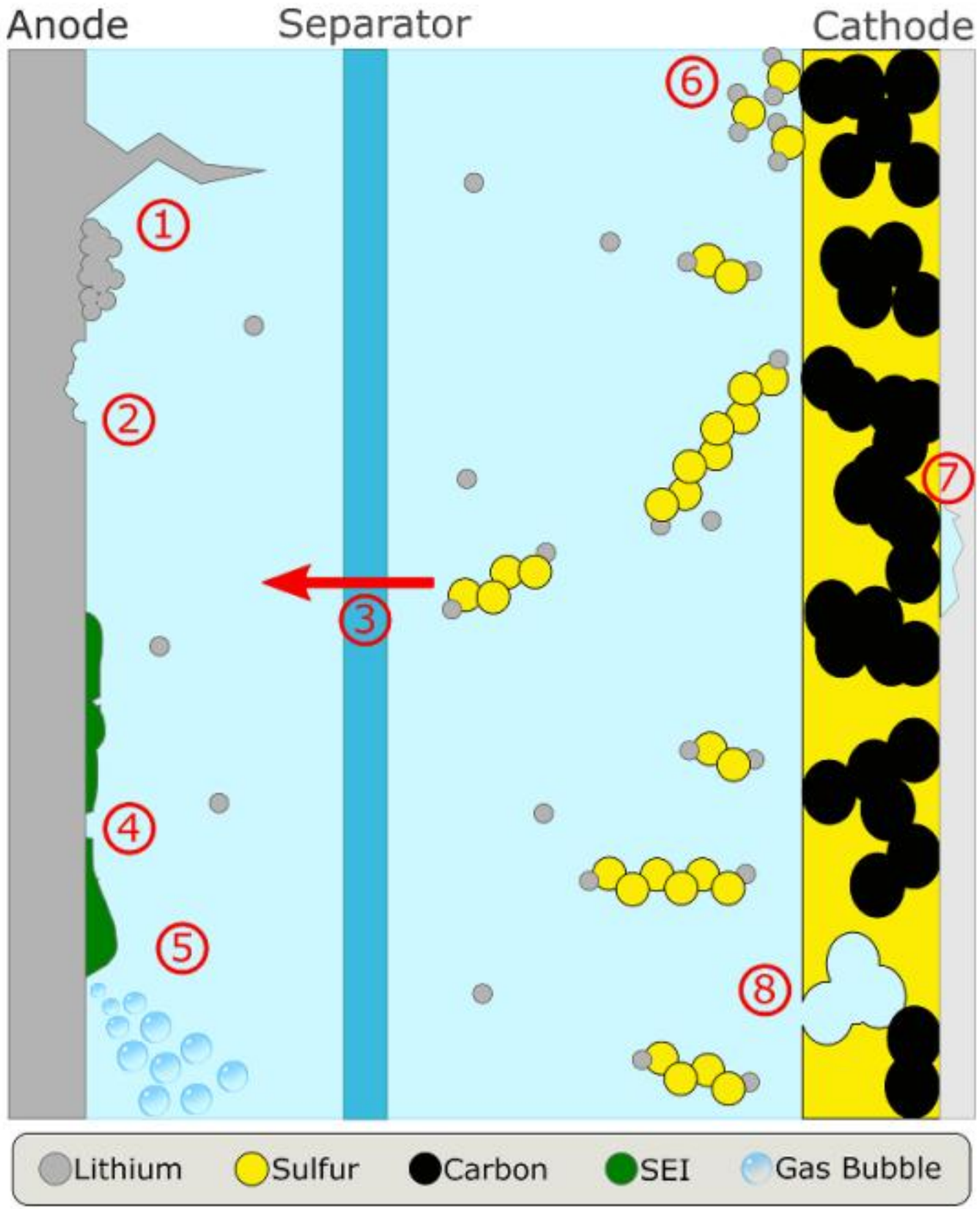

Figure 25. Schematic overview of the degradation processes in Li–S cells, many of which can lead to cell failure and safety issues.

unreacted metallic Li^0 trapped in SEI. (b) Li deposits with granular size and less tortuosity tend to maintain a good structural electronic connection, in which only small amounts of metallic Li^0 are stuck in tortuous SEI edges. (c) An ideal Li deposit should have a columnar microstructure with a large granular size, minimum tortuosity and homogeneous distribution of SEI components, facilitating a complete dissolution of metallic Li^0. Reprinted by permission from Springer Nature Customer Service Centre GmbH: Springer Nature, Nature [44]. Quantifying inactive lithium in lithium metal batteries, C. Fang et al. © 2019.

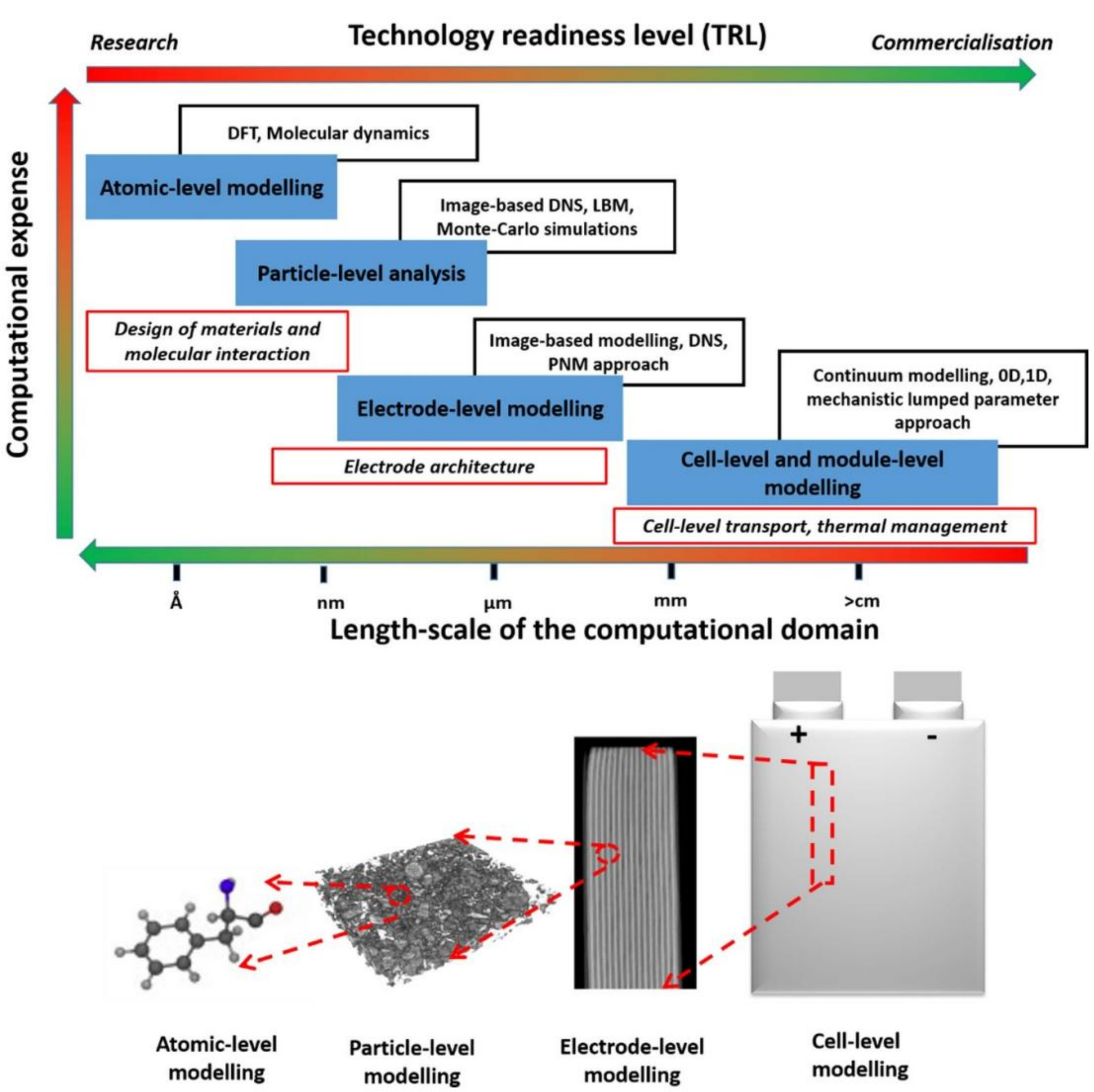

Figure 19. Multiscale modelling platform for LiSB modelling. This provides an overview of the cost and length scales

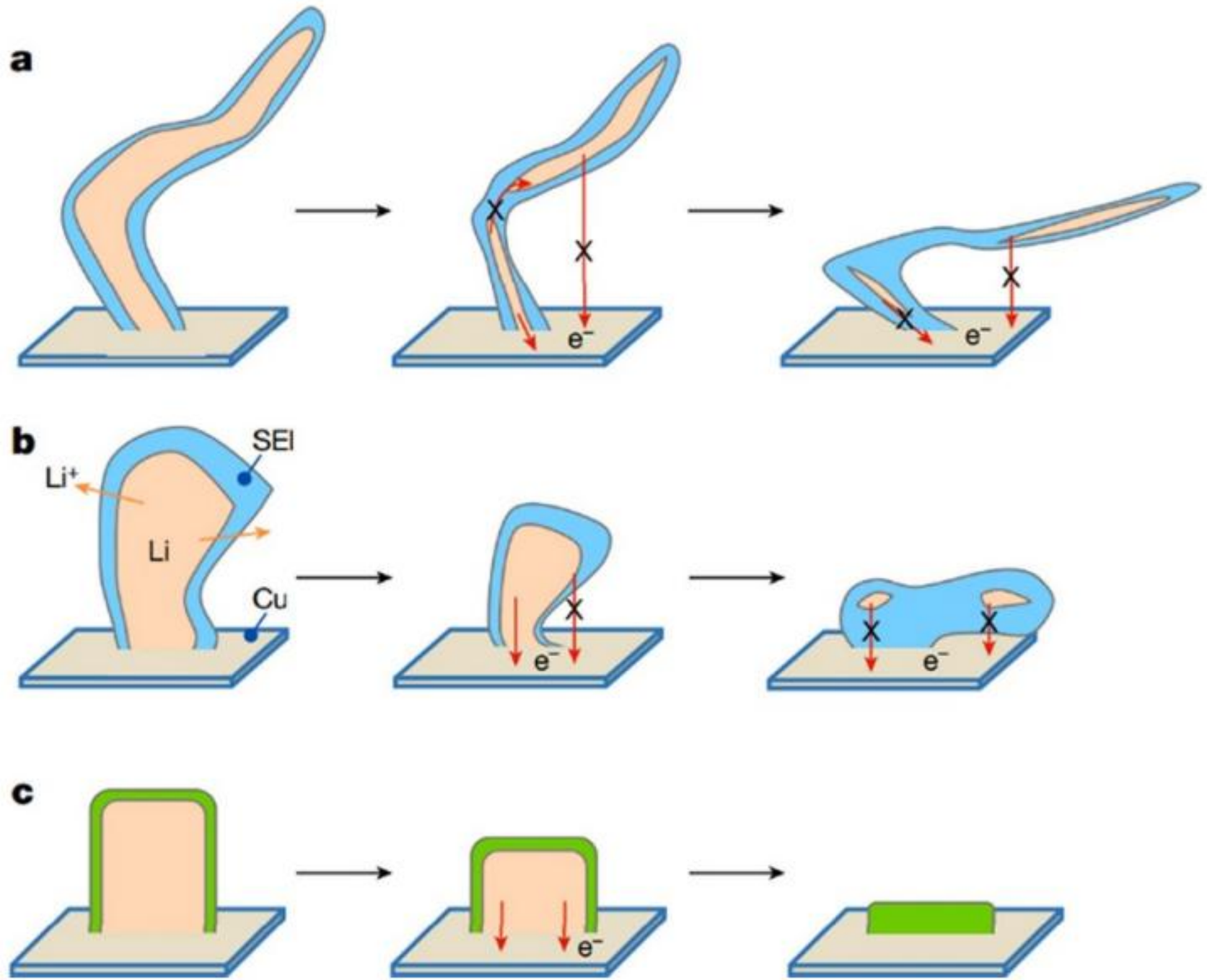

Figure 5. Schematic of inactive Li formation mechanism in different electrolytes. (a) Li deposits with whisker morphology and high tortuosity are more likely to lose electronic connection and maintain poor structural connection, leaving large amounts of unreacted metallic Li^0 trapped in SEI. (b) Li deposits with granular size and less tortuosity tend to maintain a good structural

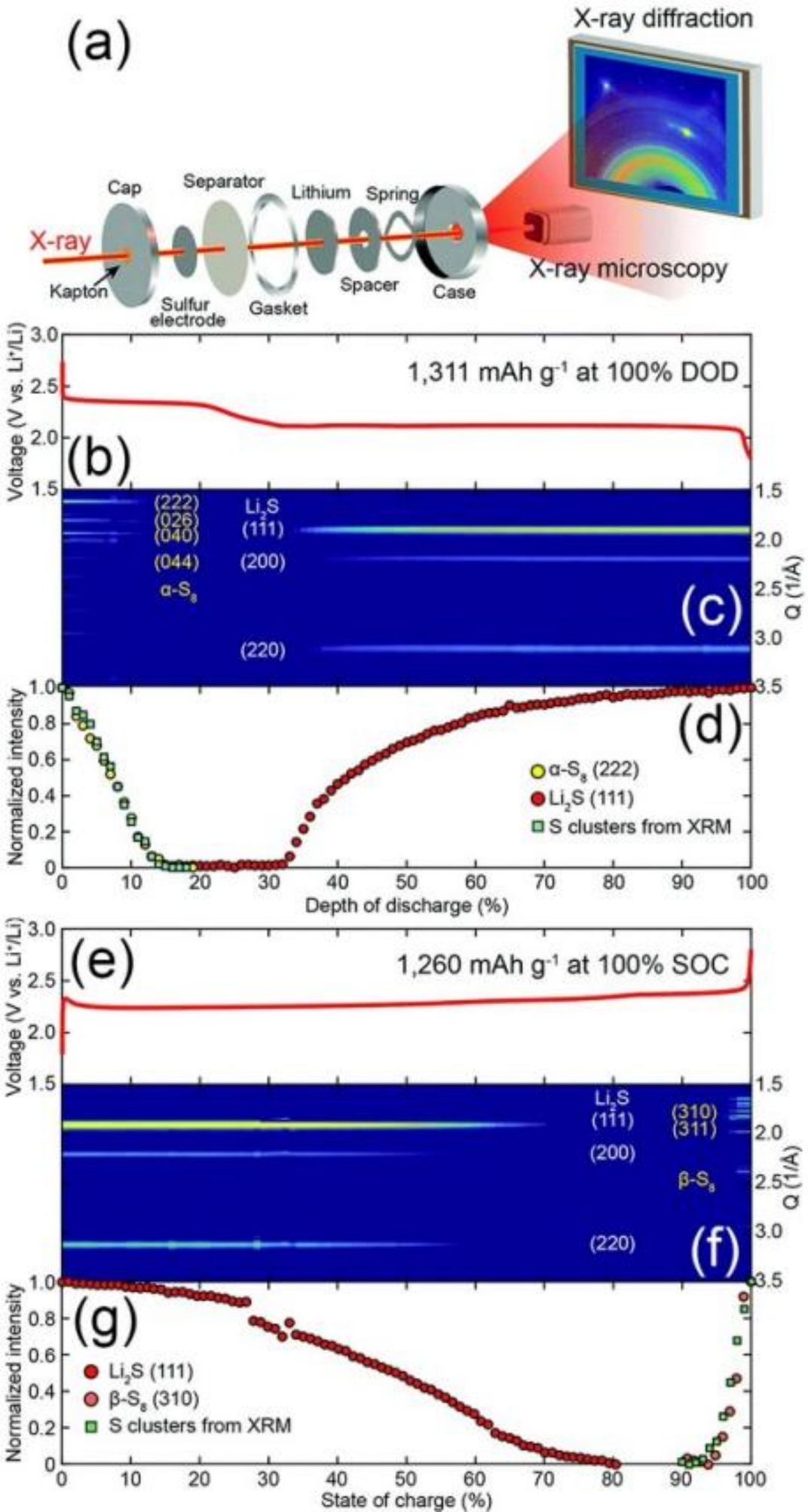
(a)
X-ray diffraction
Cap
Separator
Lithium
Spring
X-ray
Kapton
Sulfur electrode
Gasket
Spacer
Case
X-ray microscopy
(b)
1,311 mAh g-1 at 100% DOD
Voltage (V vs. Li+/Li)
(222)
(026)
(040)
(044)
α-S8
Li2S
(111)
(200)
(220)
(c)
Q (1/Å)
(d)
Normalized intensity
α-S8 (222)
Li2S (111)
S clusters from XRM
Depth of discharge (%)
(e)
1,260 mAh g-1 at 100% SOC
(310)
(311)
β-S8
(f)
(g)
β-S8 (310)
State of charge (%)

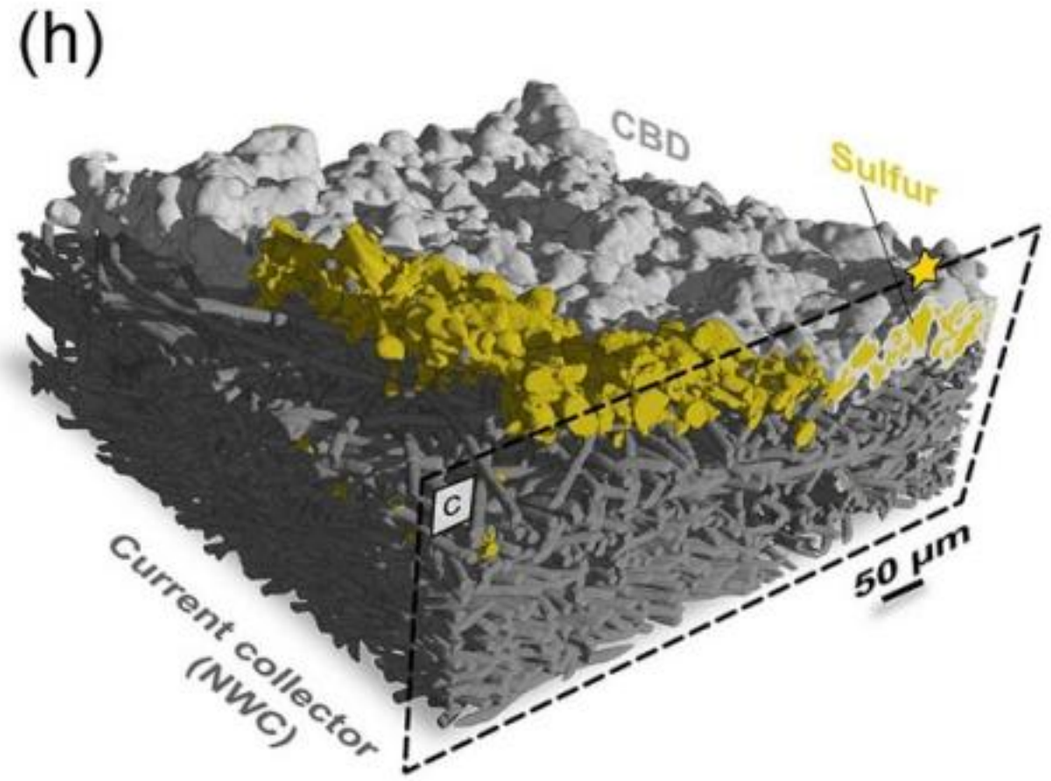
(h)
CBD
Sulfur
C
Current collector (NWC)
50 µm

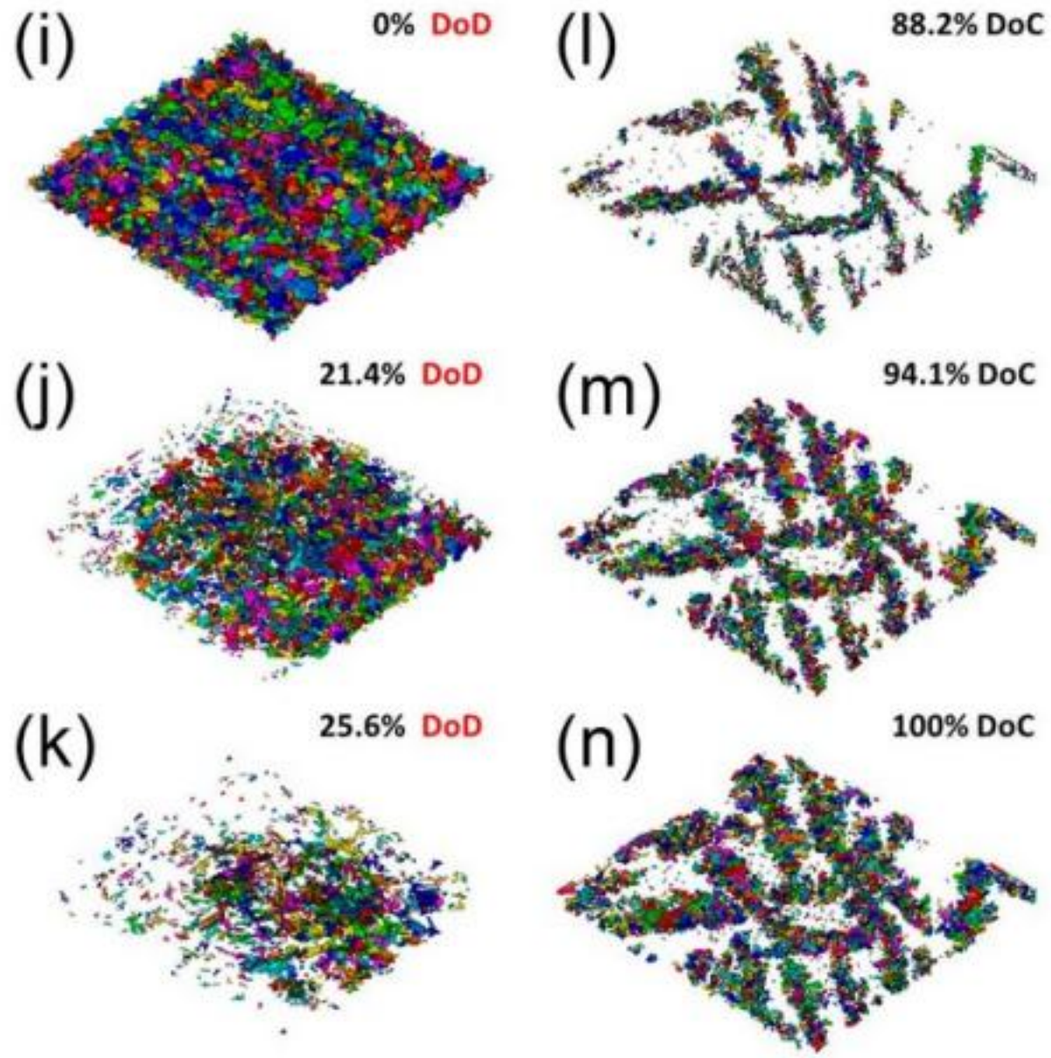
(i)
0% DoD
(l)
88.2% DoC
(j)
21.4% DoD
(m)
94.1% DoC
(k)
25.6% DoD
(n)
100% DoC

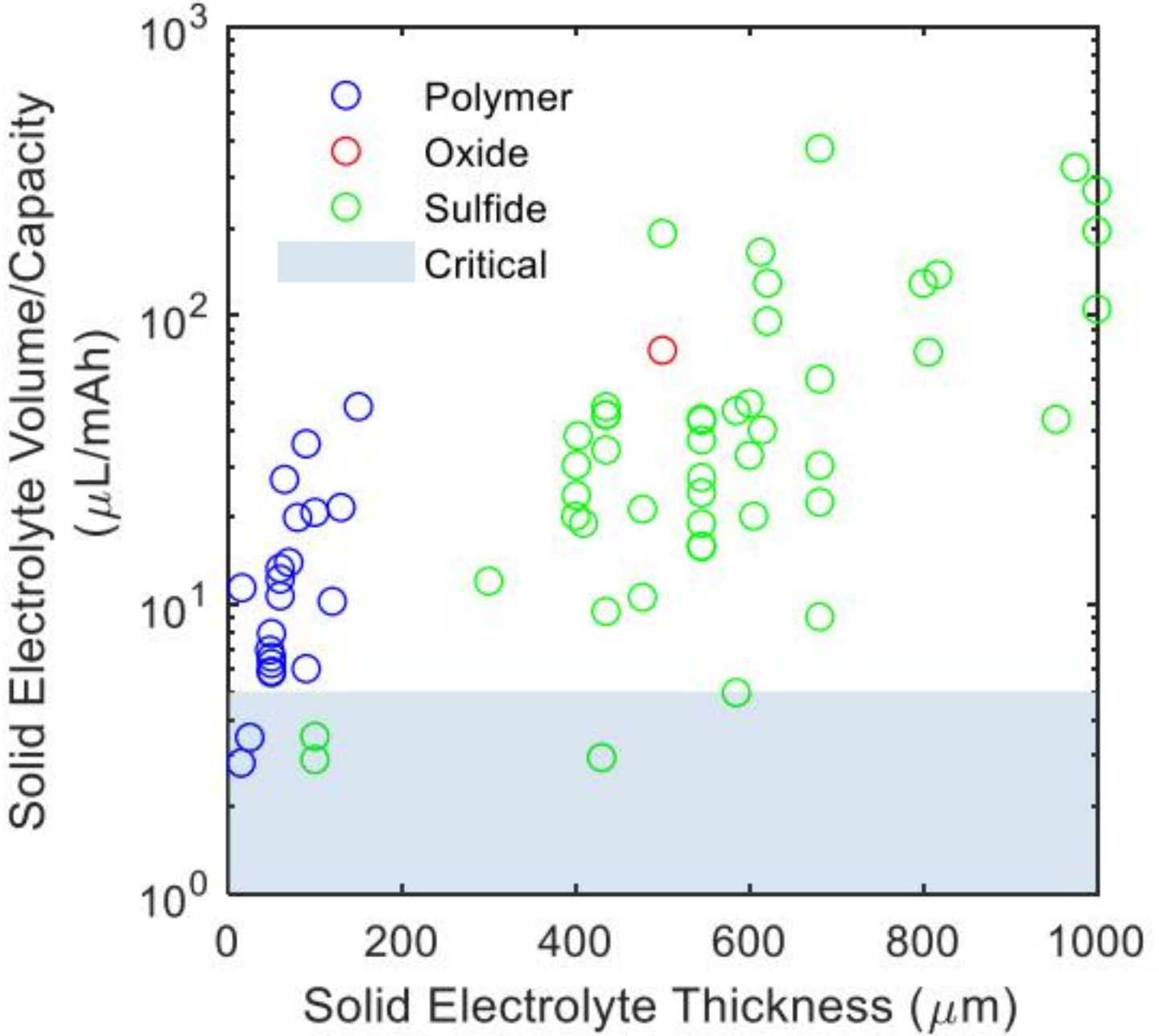
Polymer
Oxide
Sulfide
Critical
Solid Electrolyte Volume/Capacity
(μL/mAh)
Solid Electrolyte Thickness (μm)
10^3
10^2
10^1
10^0
0
200
400
600
800
1000

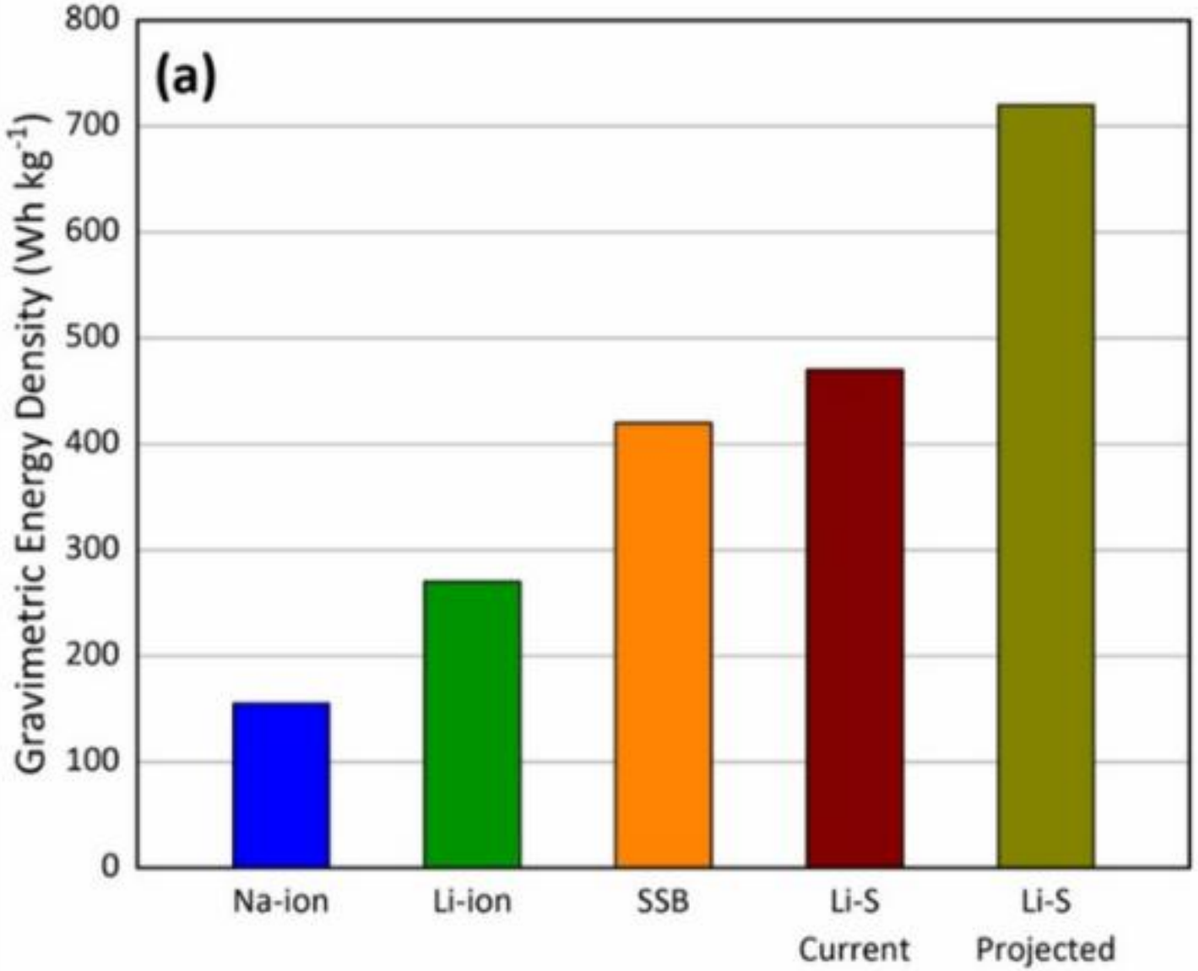

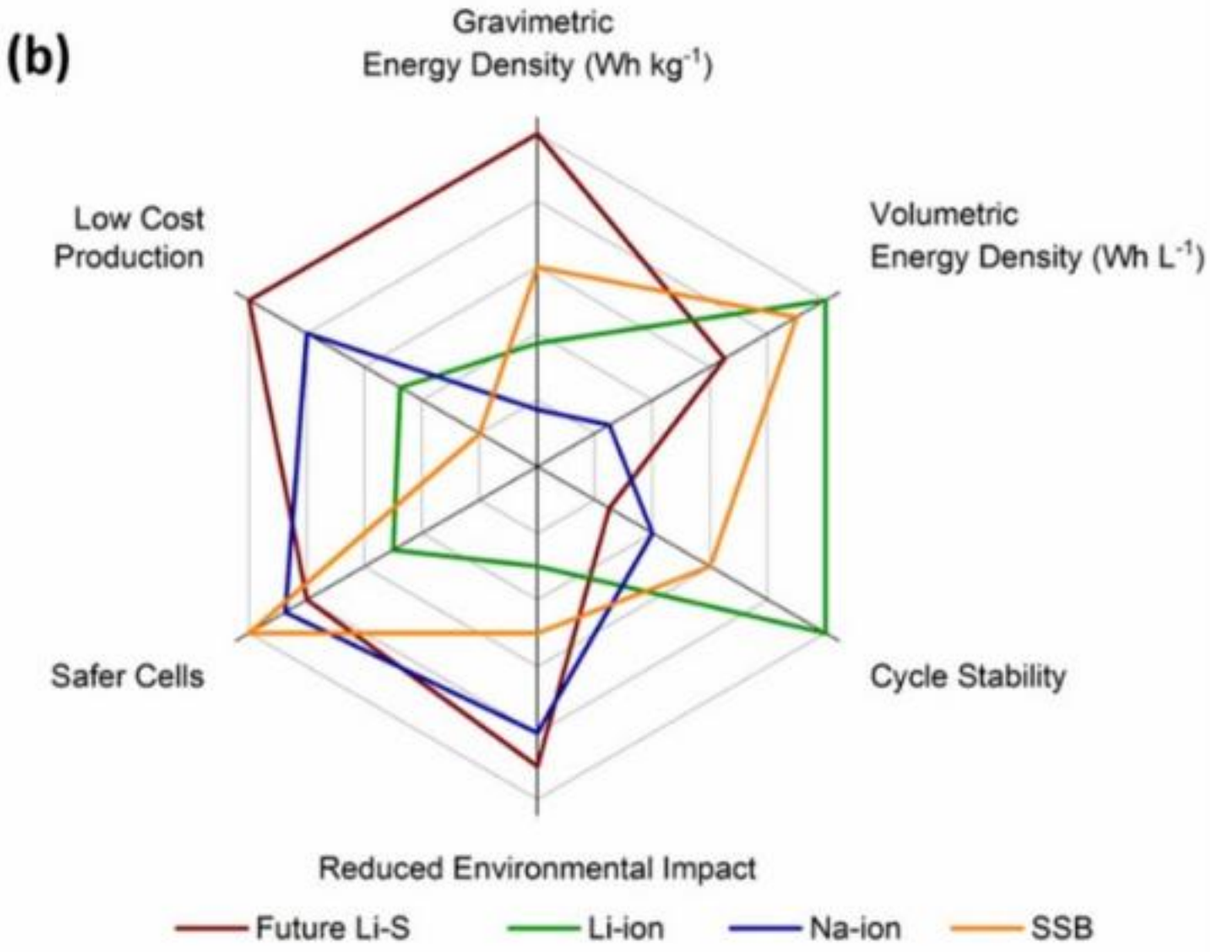

Figure 29. (a) Comparison of the predicted and demonstrated gravimetric energy density of Li–S cells compared to alternative battery technologies and (b) indicative overview of the strengths of a range of commercial or near-commercial battery

Figure 15. Typical example of a LiSB with a coated separator. (a) Cross-sectional SEM image of the interface between the carbon black-coated separator and the cathode (60 wt% S). (b) Li–S cell cycling stability comparison at cycle rate C/5 of different C nanomaterial coatings on separators. Reproduced from [101] with permissions of The Royal Society of Chemistry.

Figure 4. Predicted gravimetric energy density based on the total mass of a cathode containing S, carbon matrix, carbon black and carboxymethyl cellulose-styrene-butadiene rubber (CMC-SBR) in the ratio 59:17:18:6; and volumetric energy density based on the comprehensive volume of the cathode. The insets show schematics of the difference between low porosity and high porosity. Unutilised S, carbon matrix, and deposited Li_2S_2/Li_2S layer are represented as yellow, black, and red, respectively. Reproduced from [31]. CC BY 4.0.

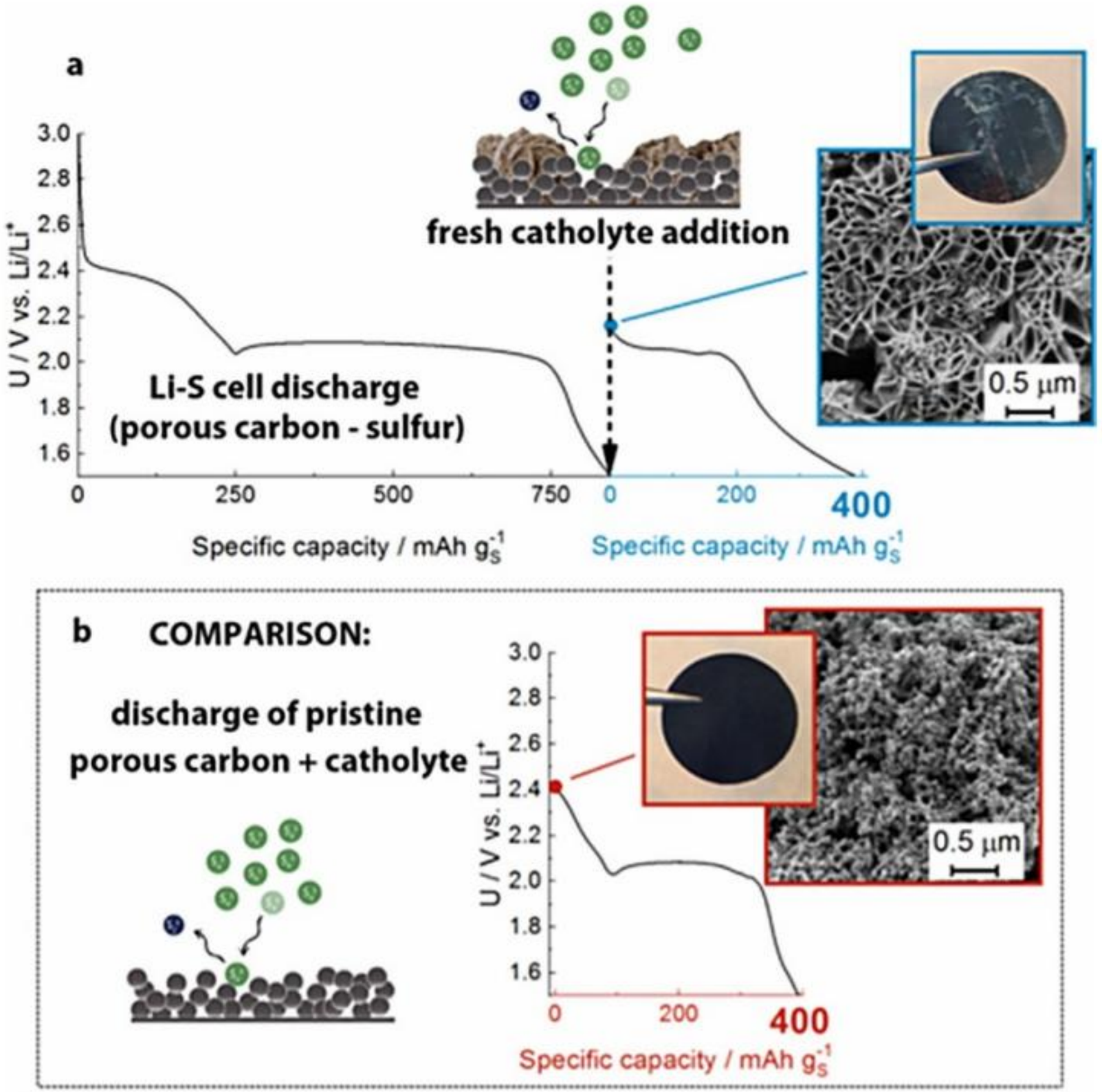

Figure 10. (a) Complete discharge of a typical LiSB followed by the addition of a fresh catholyte solution (0.1 M Li_2S_8) creating an additional discharge capacity and (b) a control experiment looking at the discharge capacity of the added catholyte solution with a porous carbon electrode [68]. Reprinted with permission from [68]. © 2019 American Chemical Society.

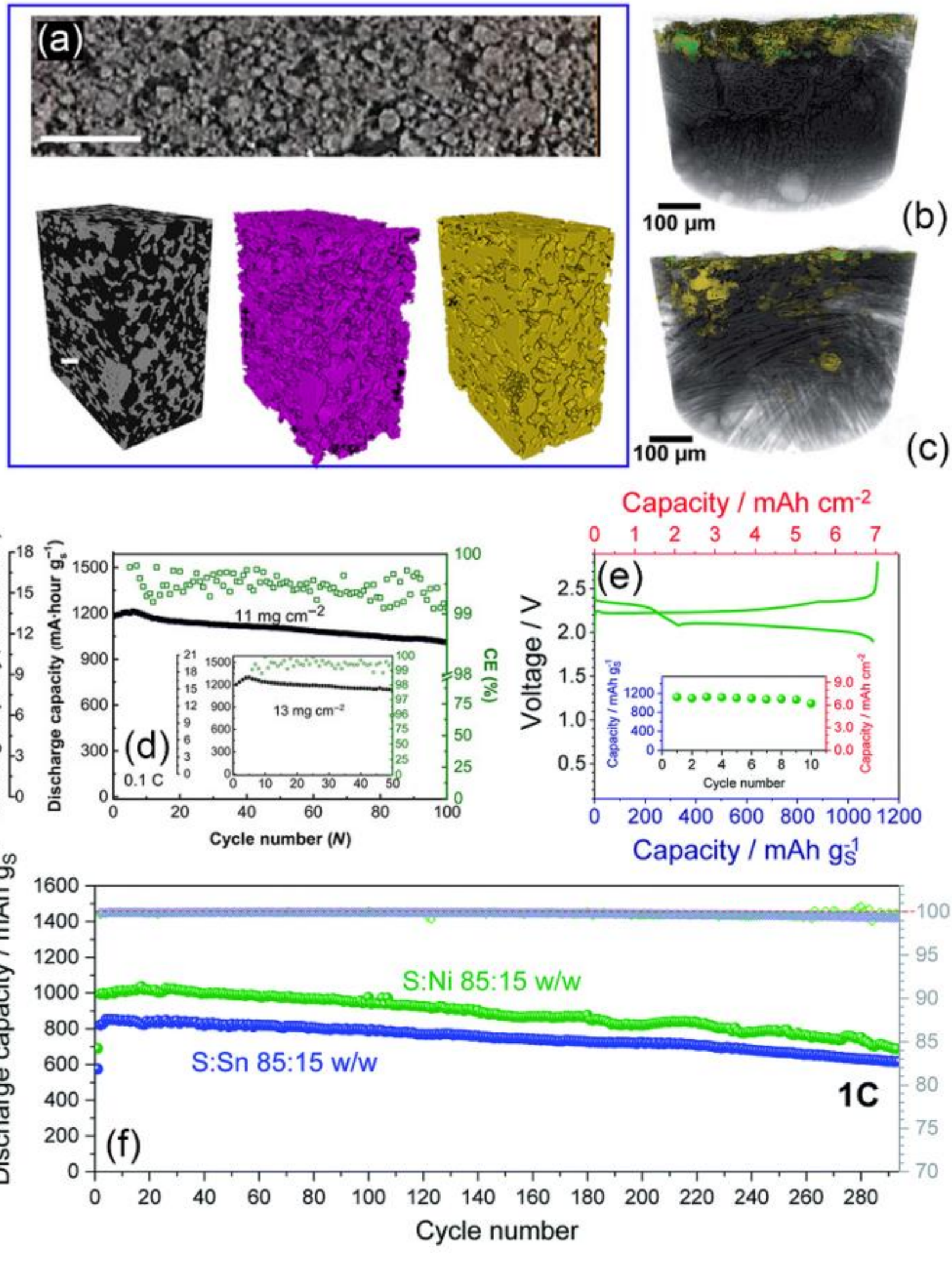

Figure 24. (a) Slice extracted from a tomographic reconstruction of an expansion-tolerant S cathode prepared by controlling the dispersion of the components and using low amounts of a high-modulus binder (top) and related volume renderings of a portio

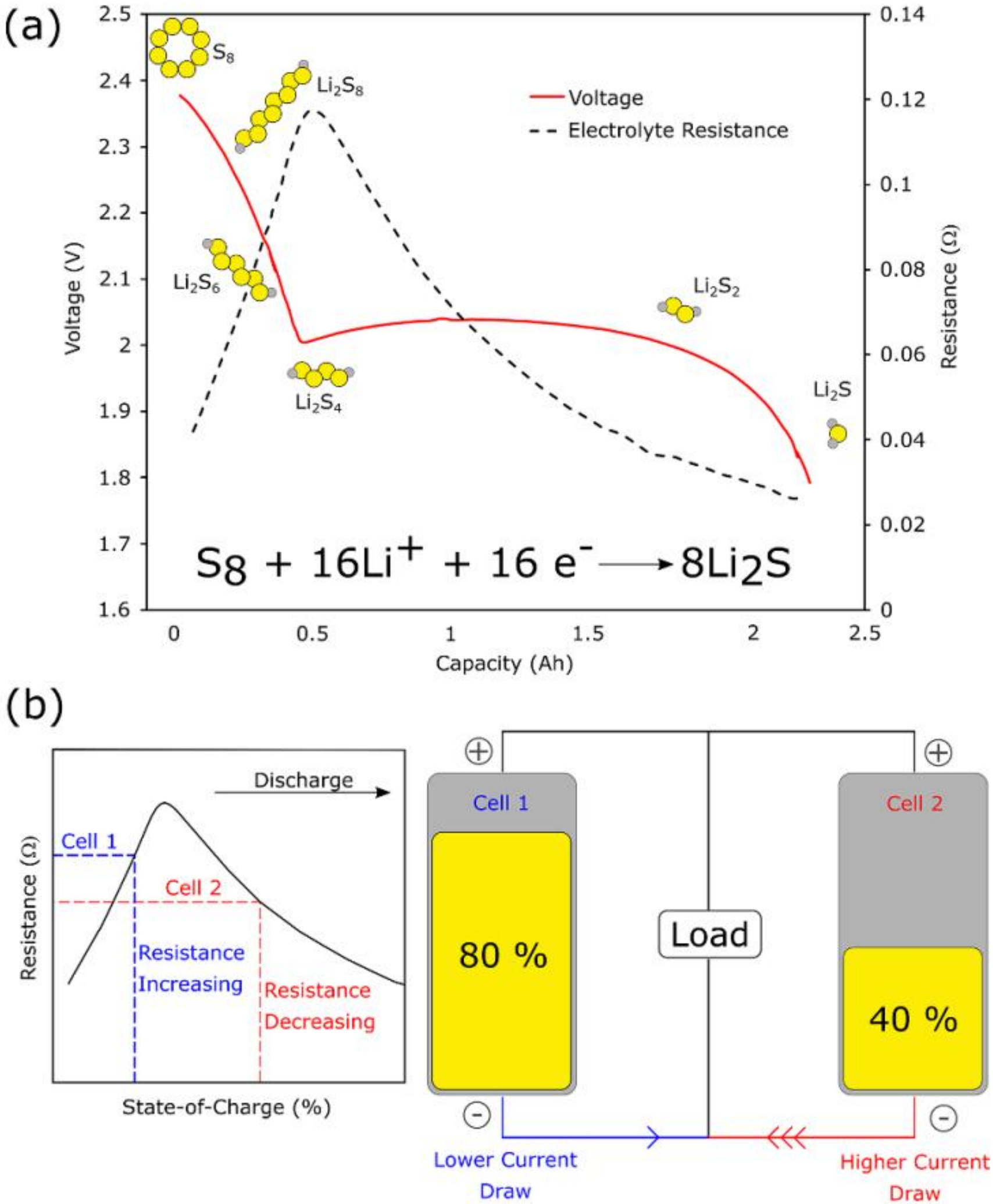

Figure 26. (a) Representation of how voltage and resistance vary in a typical LiSB during discharge. The peak in electrolyte resistance due to PS dissolution results in the observed voltage minimum between plateaus. A relatively flat voltage profile is

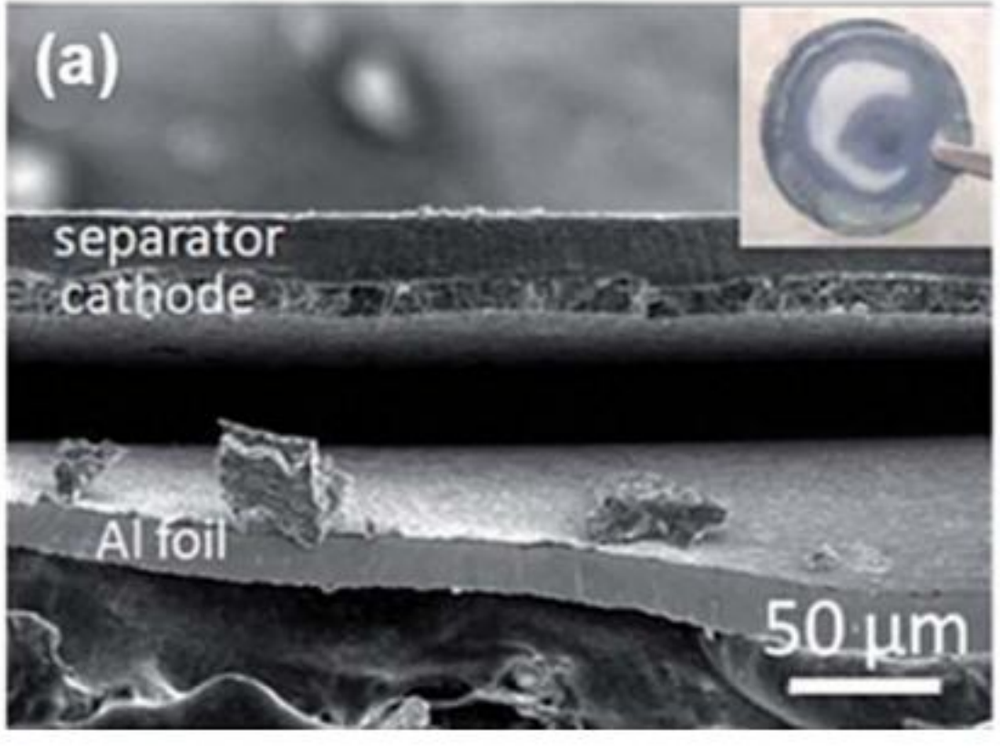
(a)
separator
cathode
Al foil
50 µm

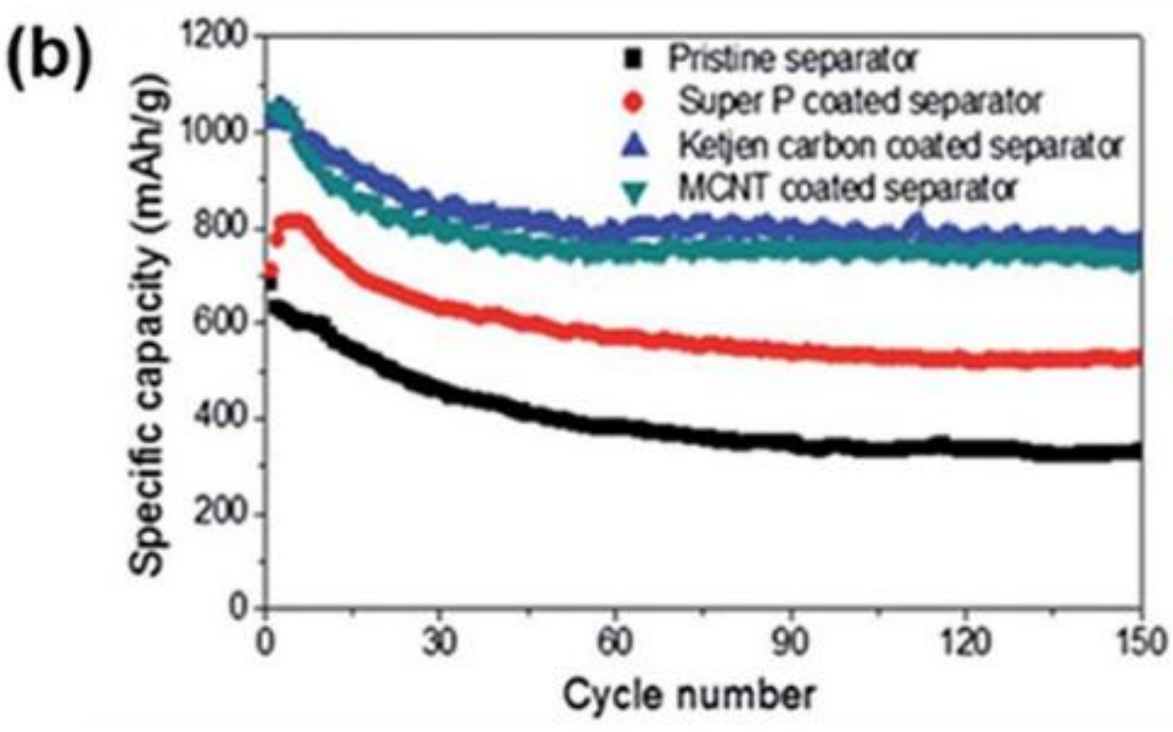
(b)
Pristine separator
Super P coated separator
Ketjen carbon coated separator
MCNT coated separator
Specific capacity (mAh/g)
Cycle number
0
200
400
600
800
1000
1200
0
30
60
90
120
150

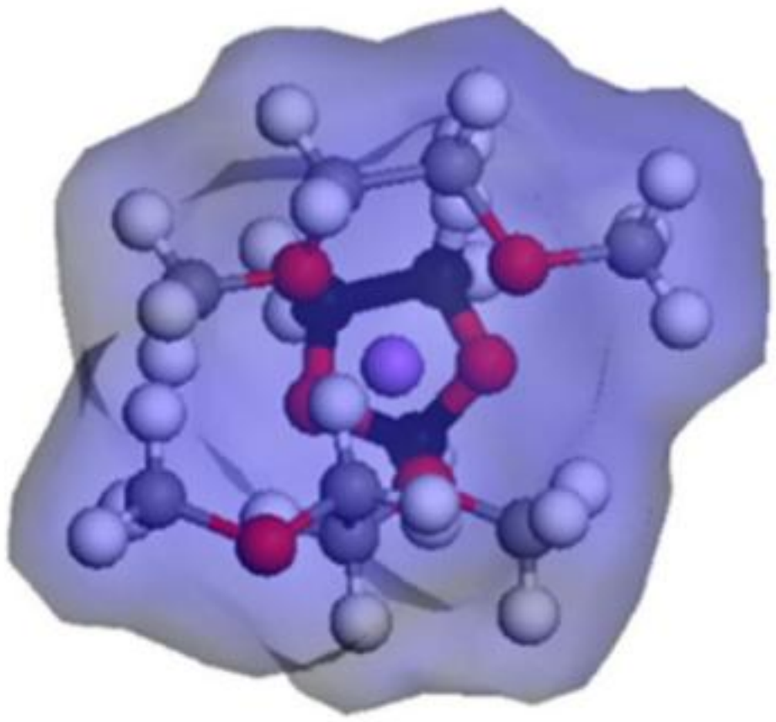

Li^+/1DOL:2DME

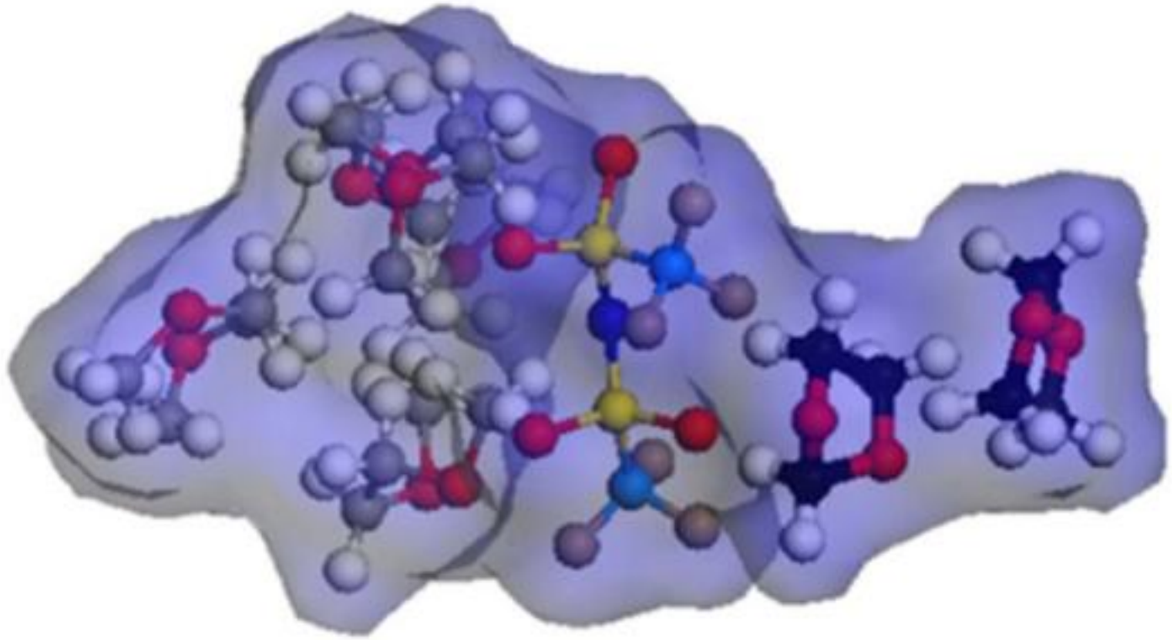

$TFSI^-$/2DOL:4DME

Figure 17. Solvated electrolyte ion structures for electrolyte LiTFSI in DOL:DME with van der Waals surface, derived from MM simulations using Materials Studio v6.1.0 and the compass force field model for the solvated Li^+ ion and the Dreiding force field model for the solvated $TFSI^-$ ion.

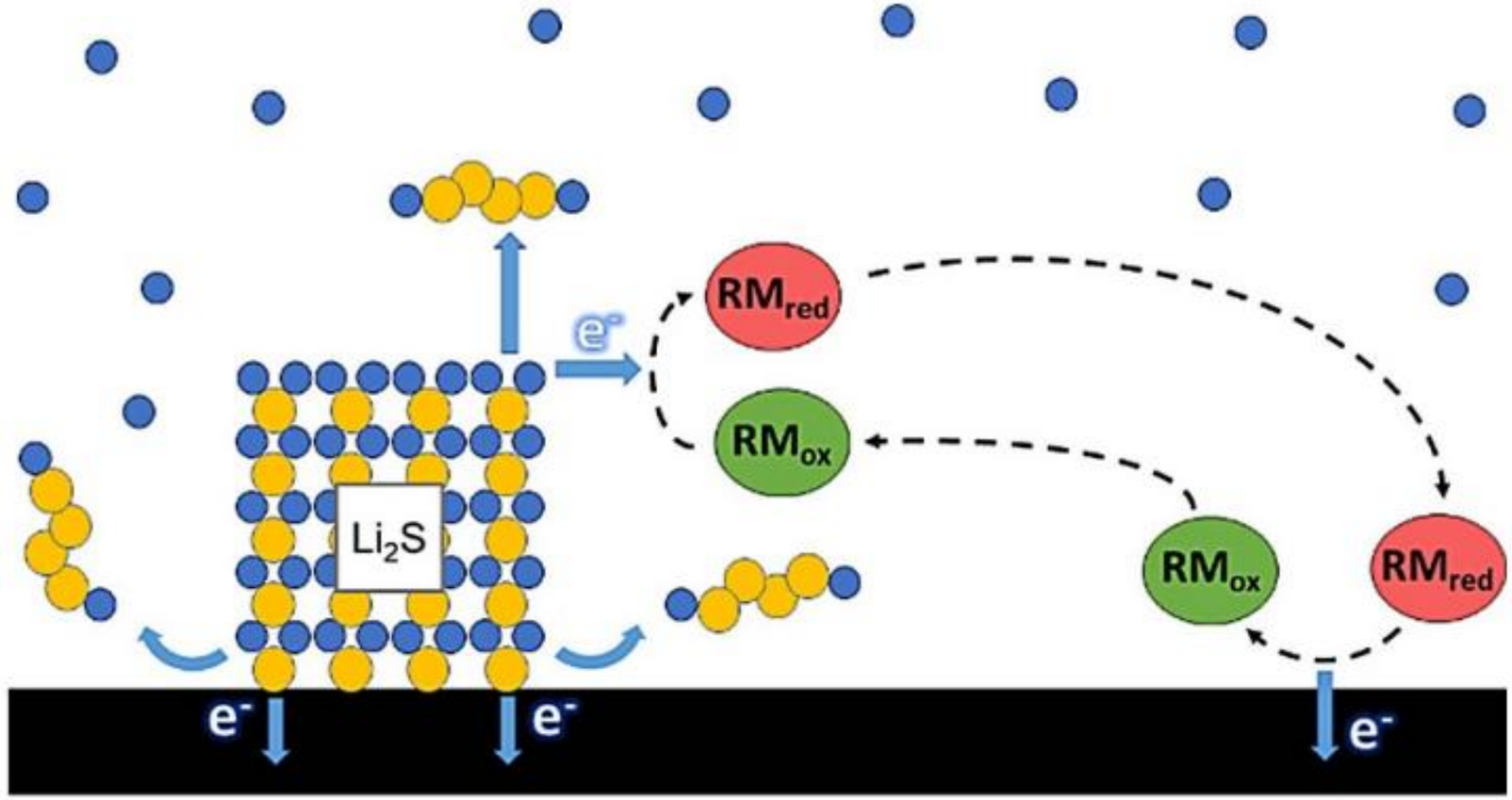

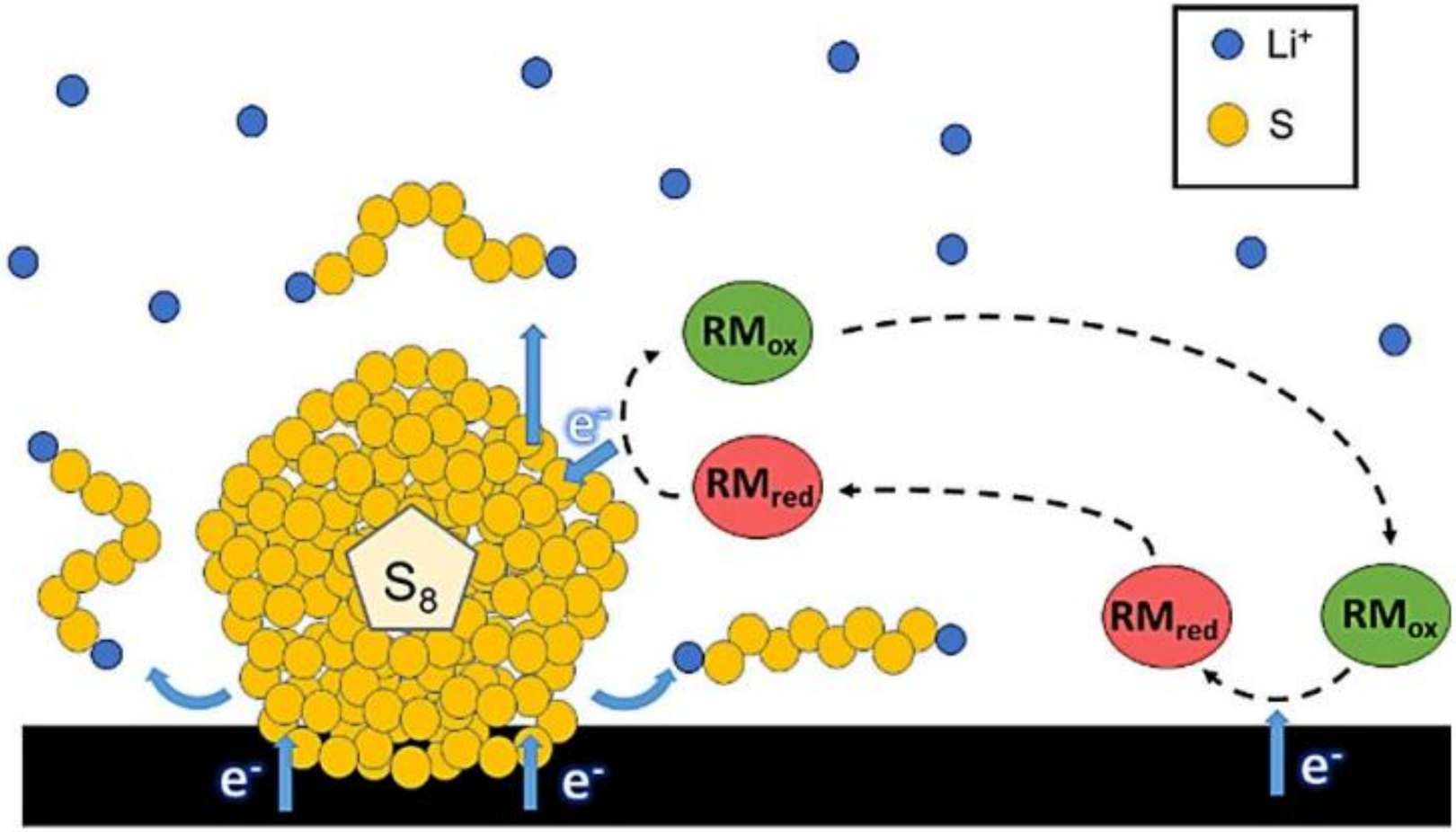

Figure 11. Schematic showing the operating principle behind the use of RMs for (a) the reduction of S_8 to long-chain PSs and (b) the oxidation of Li_2S to short-chain PSs.

Figure 9. Proposed S reduction reaction mechanism involving chemical PS reactions (VI.1 to VI.7) in the pathway of S_1^{2-} (that is, Li_2S) formation [64]. Reprinted with permission from [64]. © 2014 American Chemical Society.

Figure 27. Example of high-capacity Li–S pouch cells from OXIS Energy (top). Worldwide granted patents in the field of Li–S technology (bottom).

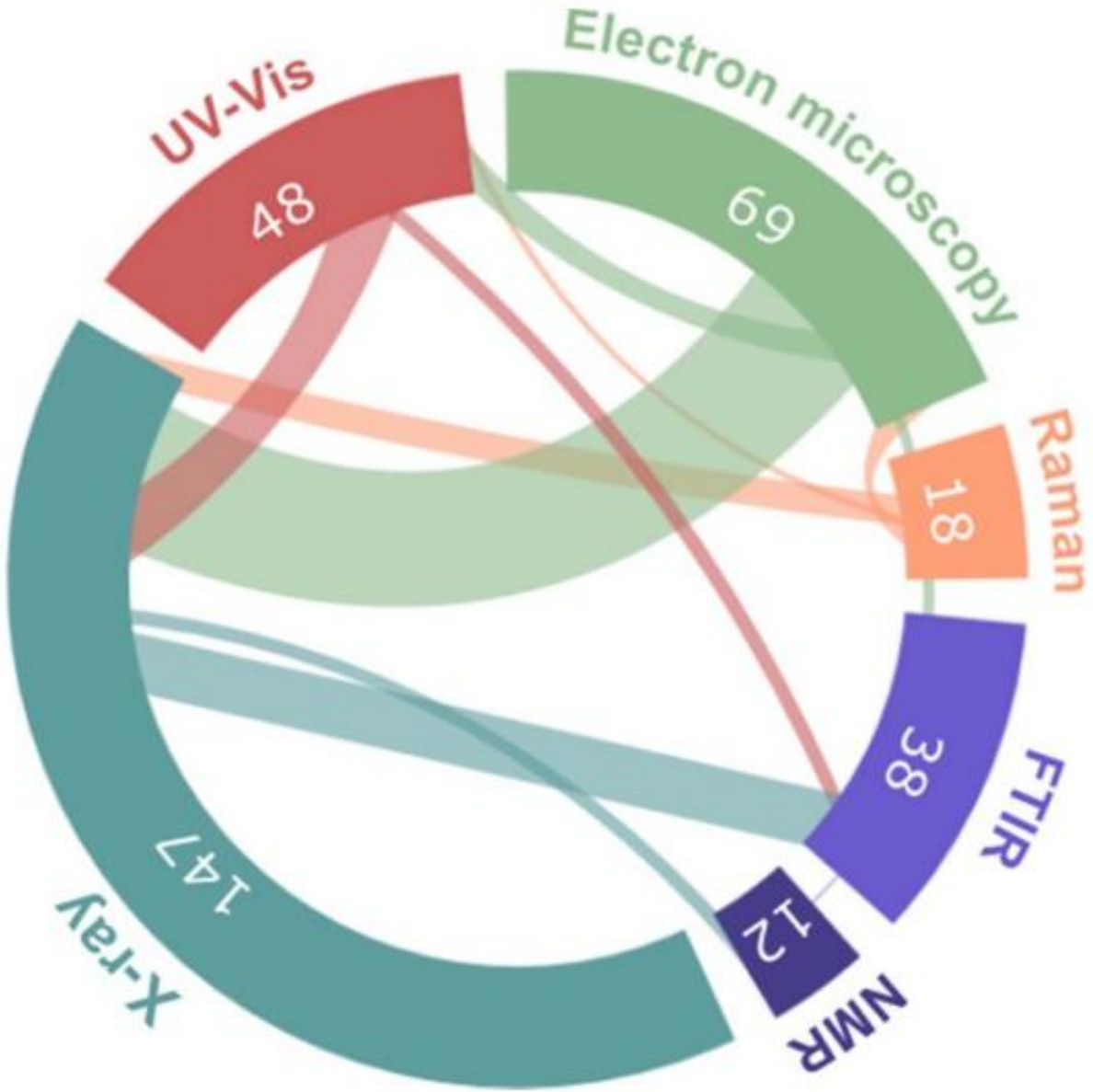

Figure 22. Number of research articles on the Web of Science database as of 2020 with 'lithium–sulfur' or 'Li–S' in the title and '*in situ*' in the title, abstract or keywords. Links show the number of articles that include both keywords.

Figure 18. Diagram of continuum volume-averaged model for an electrochemical cell including anode, separator and cathode, taking into account the PSD of the cathode, and transport of solvated (wrapped by light blue-coloured shell of solvent molecules) or desolvated ions of the electrolyte as described in [122].

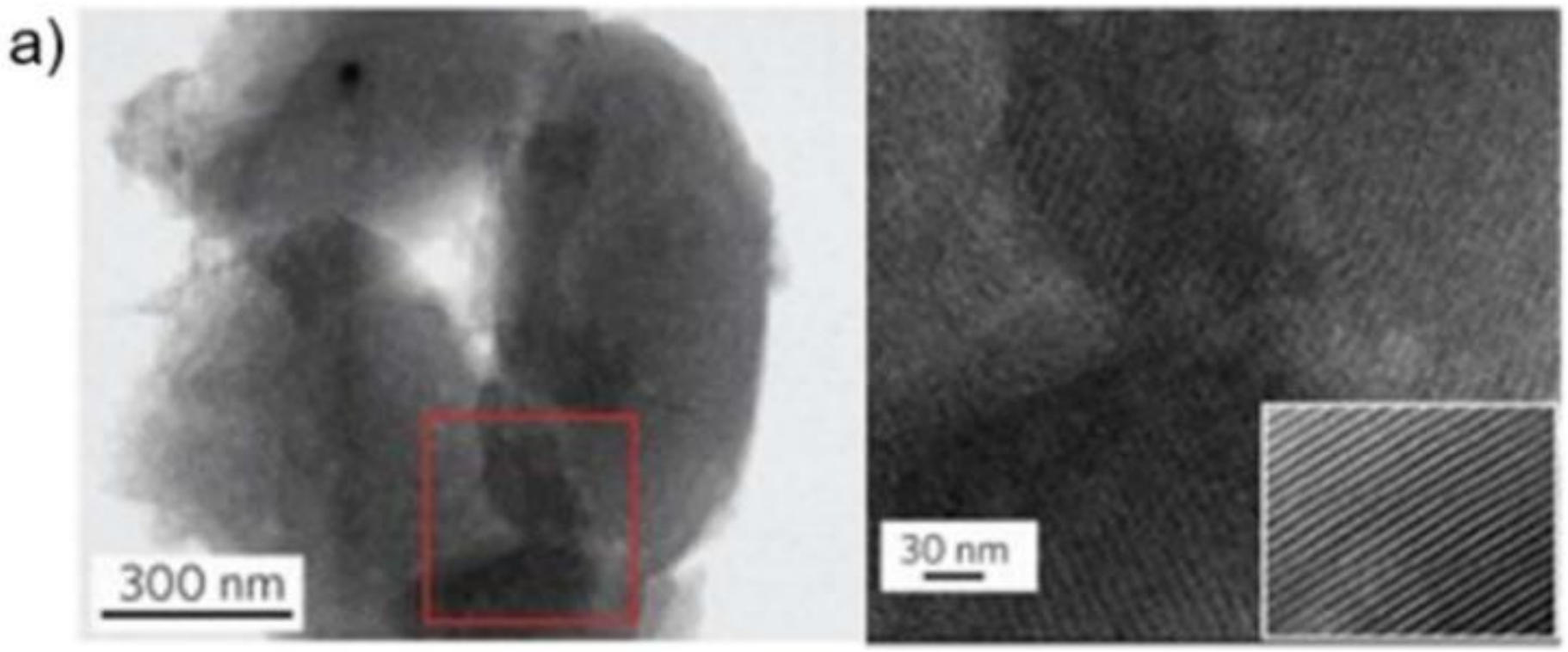

Figure 3. TEM images of different carbon morphologies used for S cathodes. (a) Ordered mesoporous carbon CMK-3/S composite particle (left), and image expansion corresponding to the area outlined by the red square (right) where the in the TEM image for pristine CMK-3 at the same magnification. Reprinted by permission from Springer Nature Custome Centre GmbH: springer Nature, Nature Materials [25] A highly ordered nanostructured carbon–sulphur cathode for

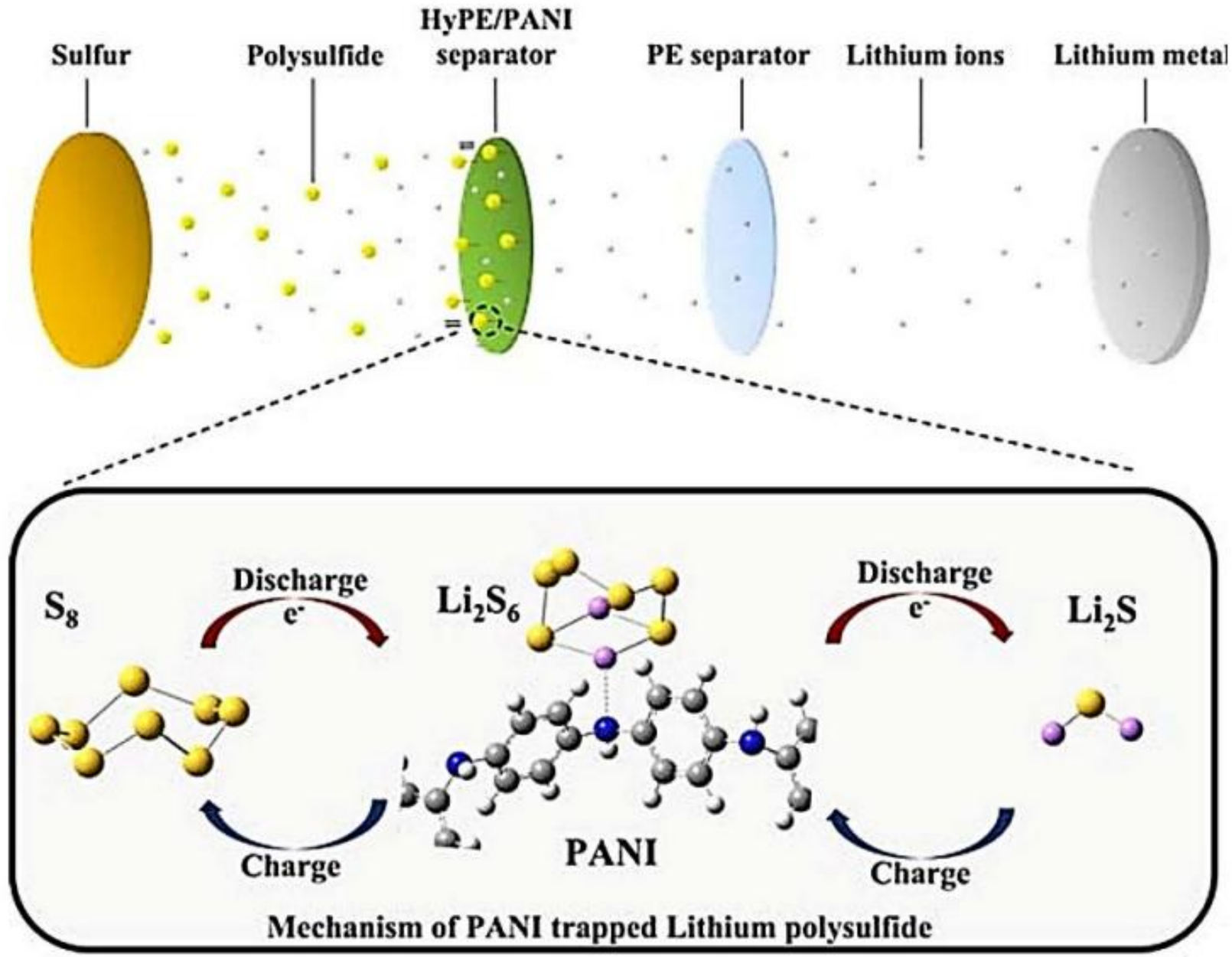

Figure 14. Li–S cell schematic with interlayer composed from hydrolysed PE and PANI. The inset displays the impact of the interlayer on the migration/diffusion of soluble PS intermediates during charge/discharge (shuttle effect). Reprinted with permission from [98]. © 2014 American Chemical Society.

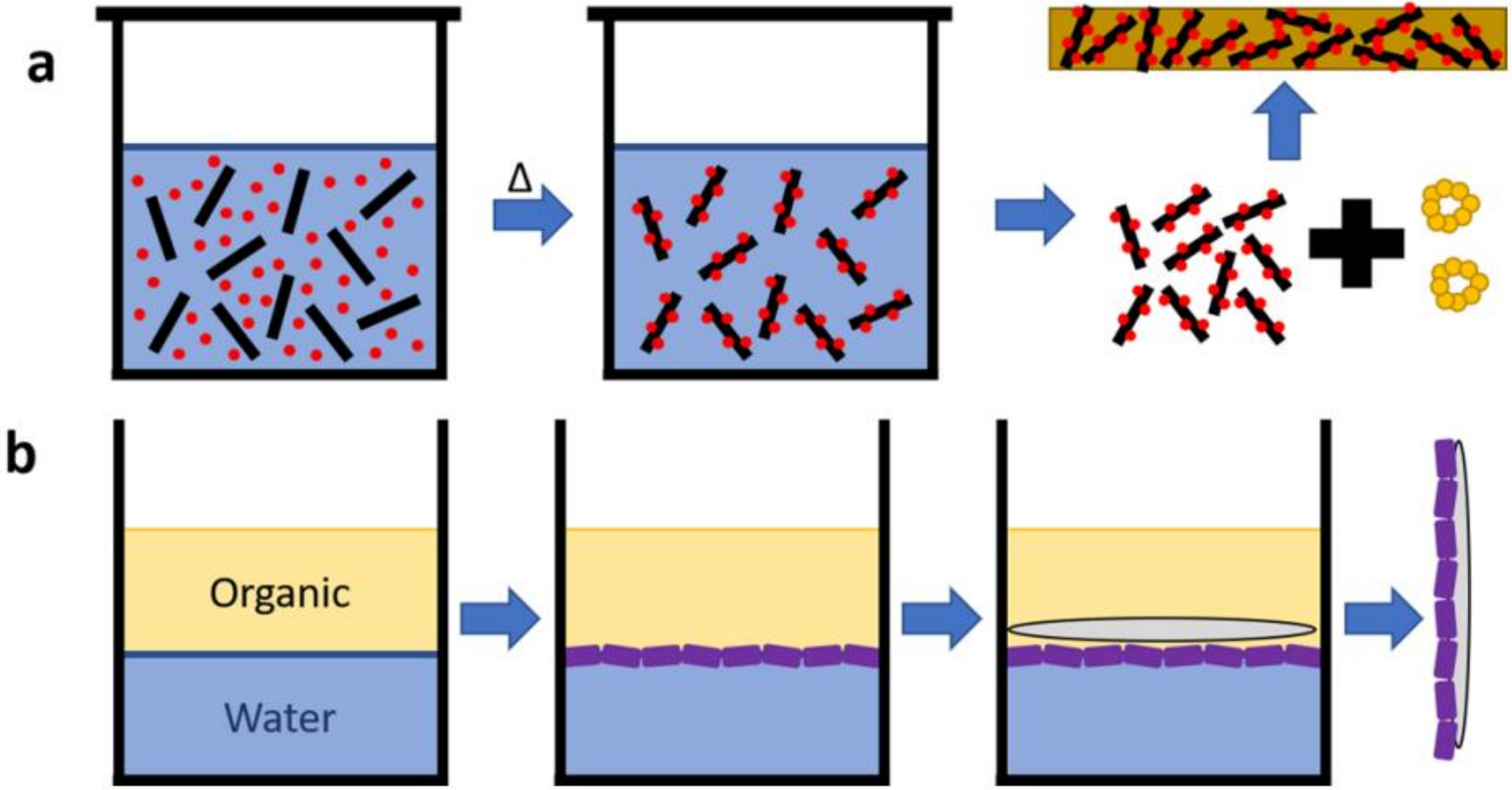
a
Δ
b
Organic
Water

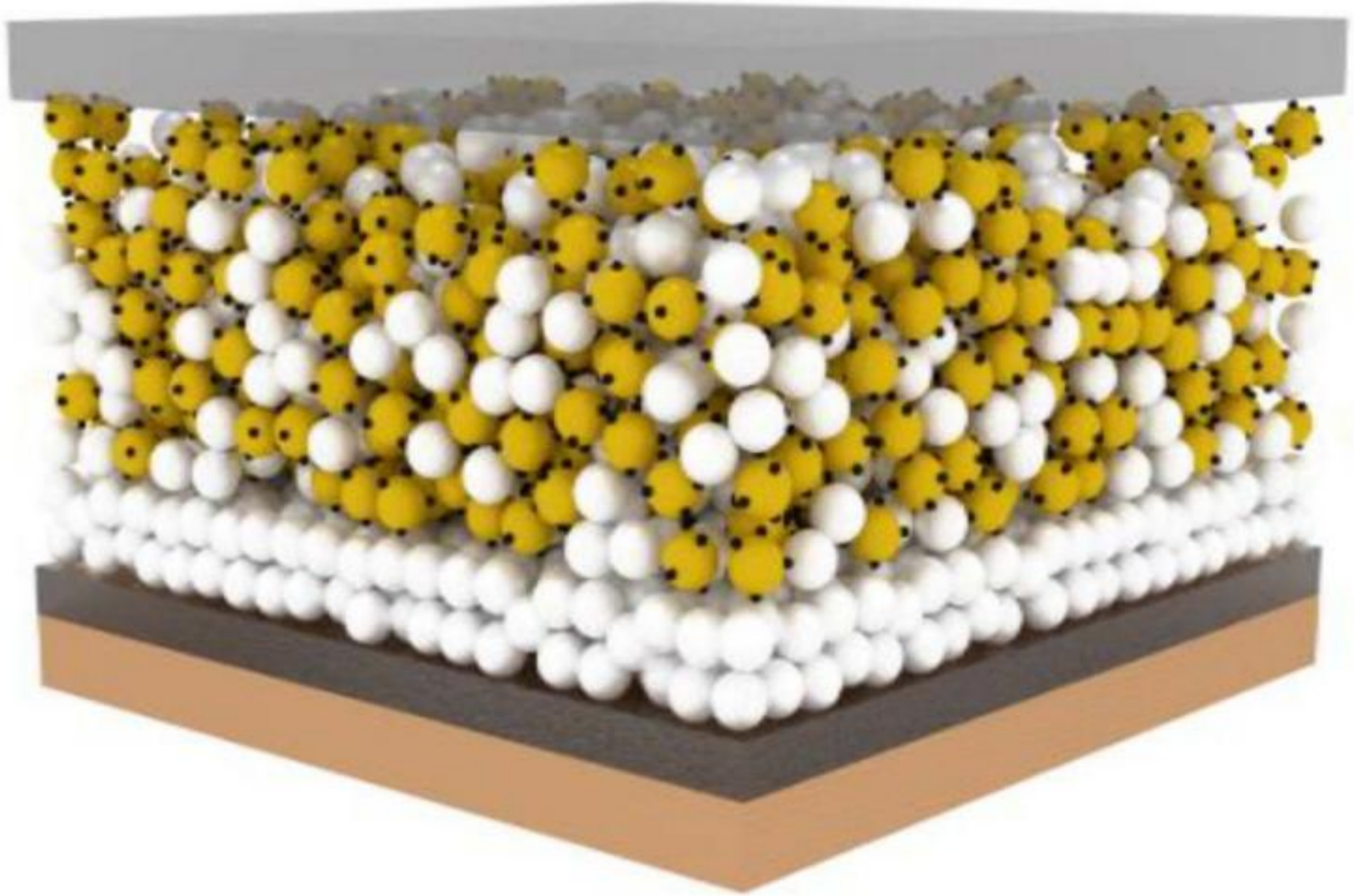

Figure 8. Illustration of an ASSLSB.

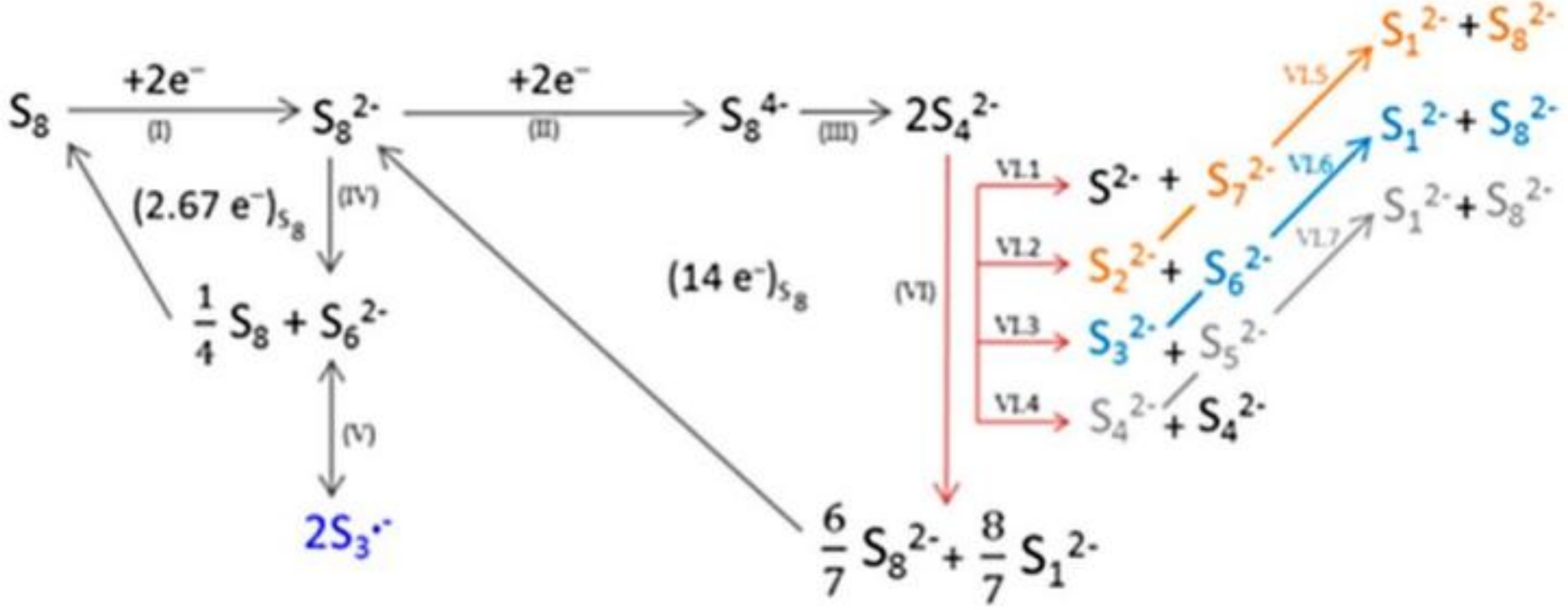
S8
+2e⁻
(I)
S8 2-
+2e⁻
(II)
S8 4-
(III)
2S4 2-
(2.67 e⁻)S8
(IV)
1/4 S8 + S6 2-
(V)
2S3 •-
(14 e⁻)S8
(VI)
VI.1
VI.2
VI.3
VI.4
S2- + S7 2-
S2 2- + S6 2-
S3 2- + S5 2-
S4 2- + S4 2-
VI.5
VI.6
VI.7
S1 2- + S8 2-
S1 2- + S8 2-
S1 2- + S8 2-
6/7 S8 2- + 8/7 S1 2-

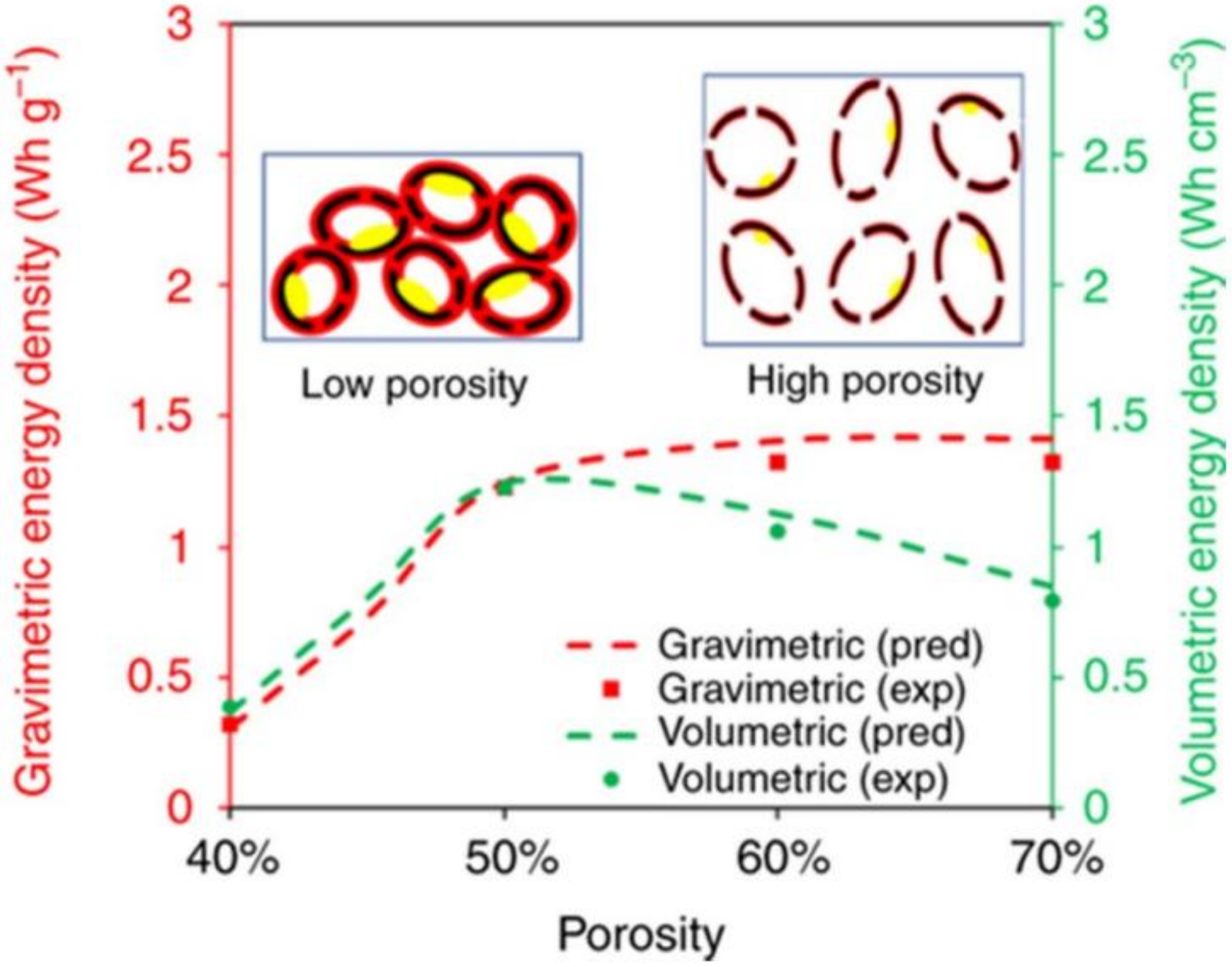
Gravimetric energy density (Wh g^{-1})
Volumetric energy density (Wh cm^{-3})
Porosity
40%
50%
60%
70%
0
0.5
1
1.5
2
2.5
3
Low porosity
High porosity
Gravimetric (pred)
Gravimetric (exp)
Volumetric (pred)
Volumetric (exp)

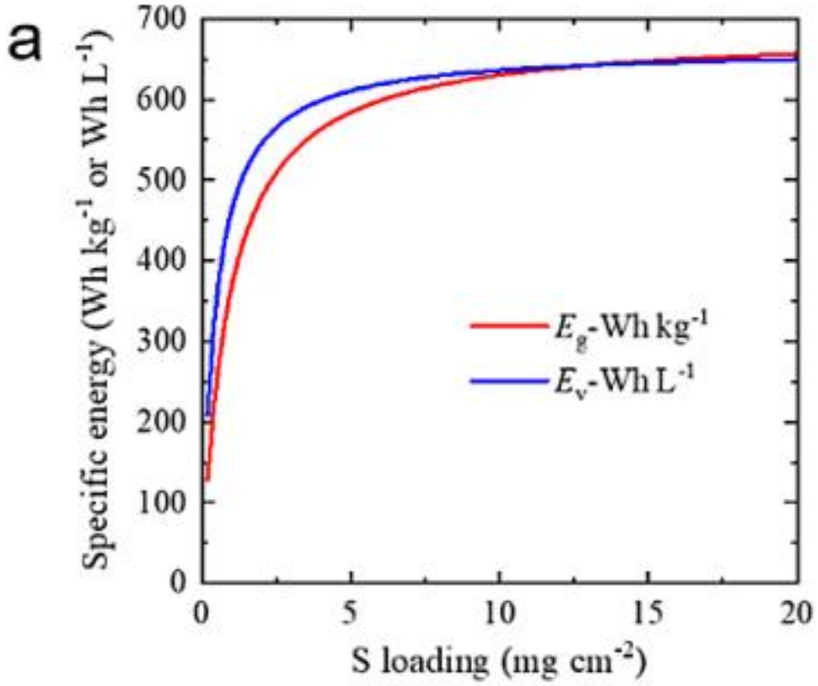

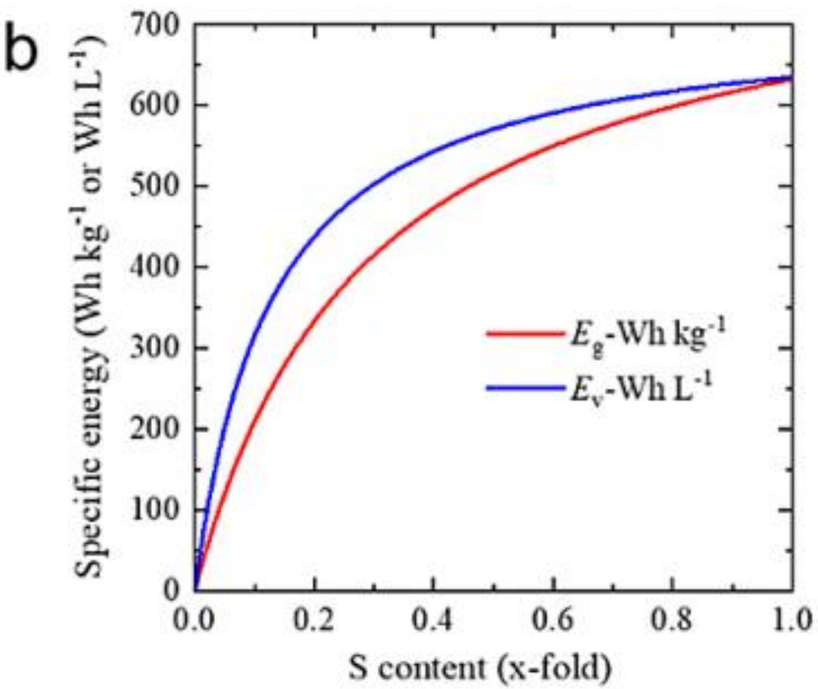

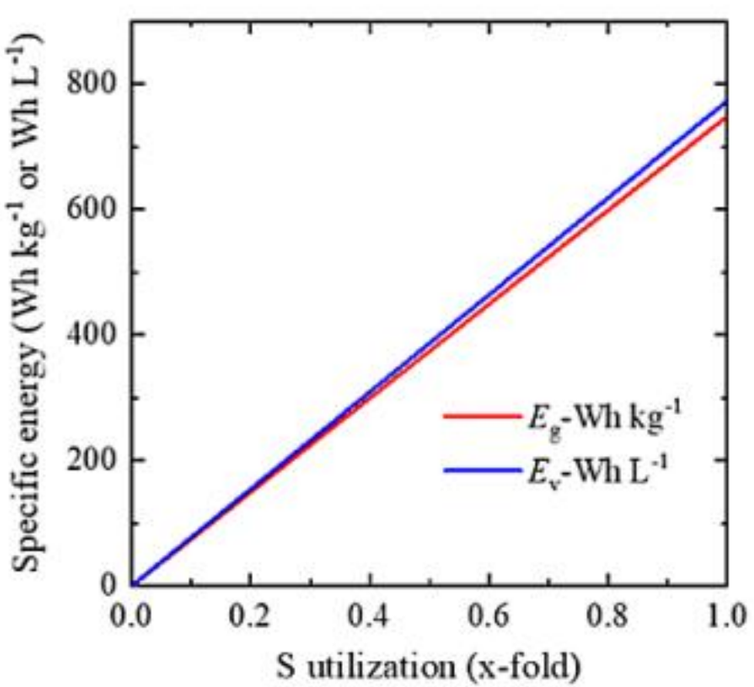

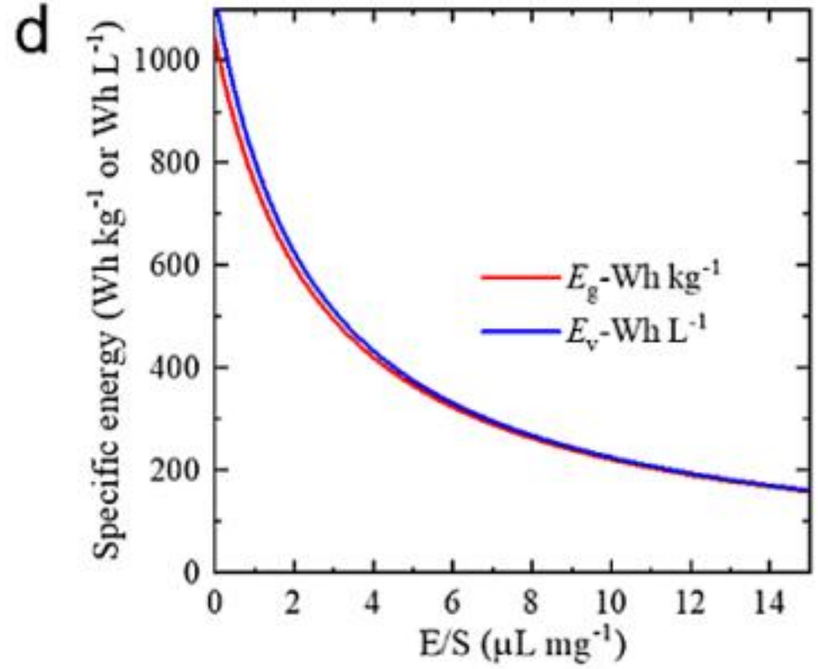

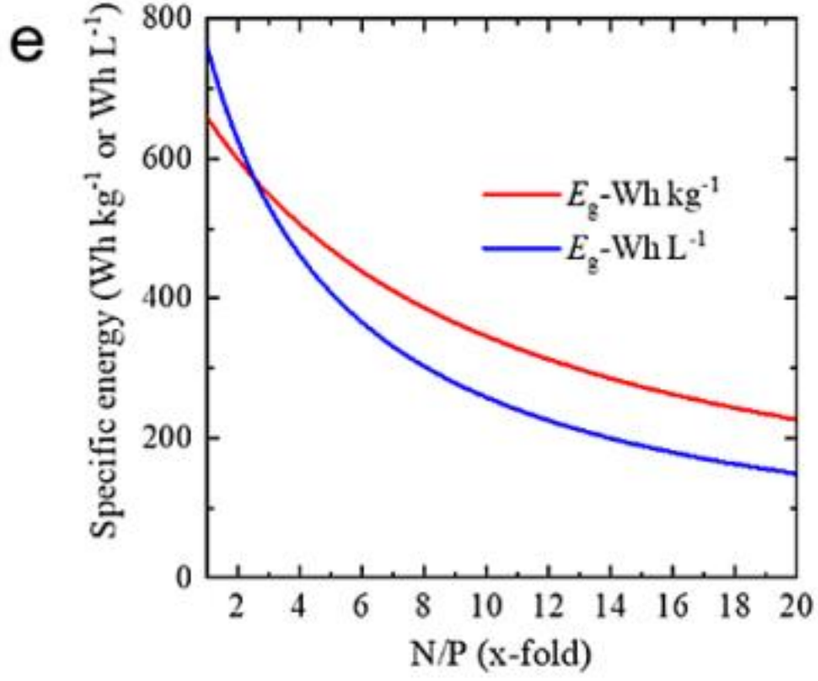

Figure 2. Predicted gravimetric and volumetric energy density from equations (1) and (2). (a) S loading, (b) S content, (c) S utilisation, (d) E/S, (e) N/P. Each graph is plotted as a function of one parameter by fixing the other four parameters. S loading:

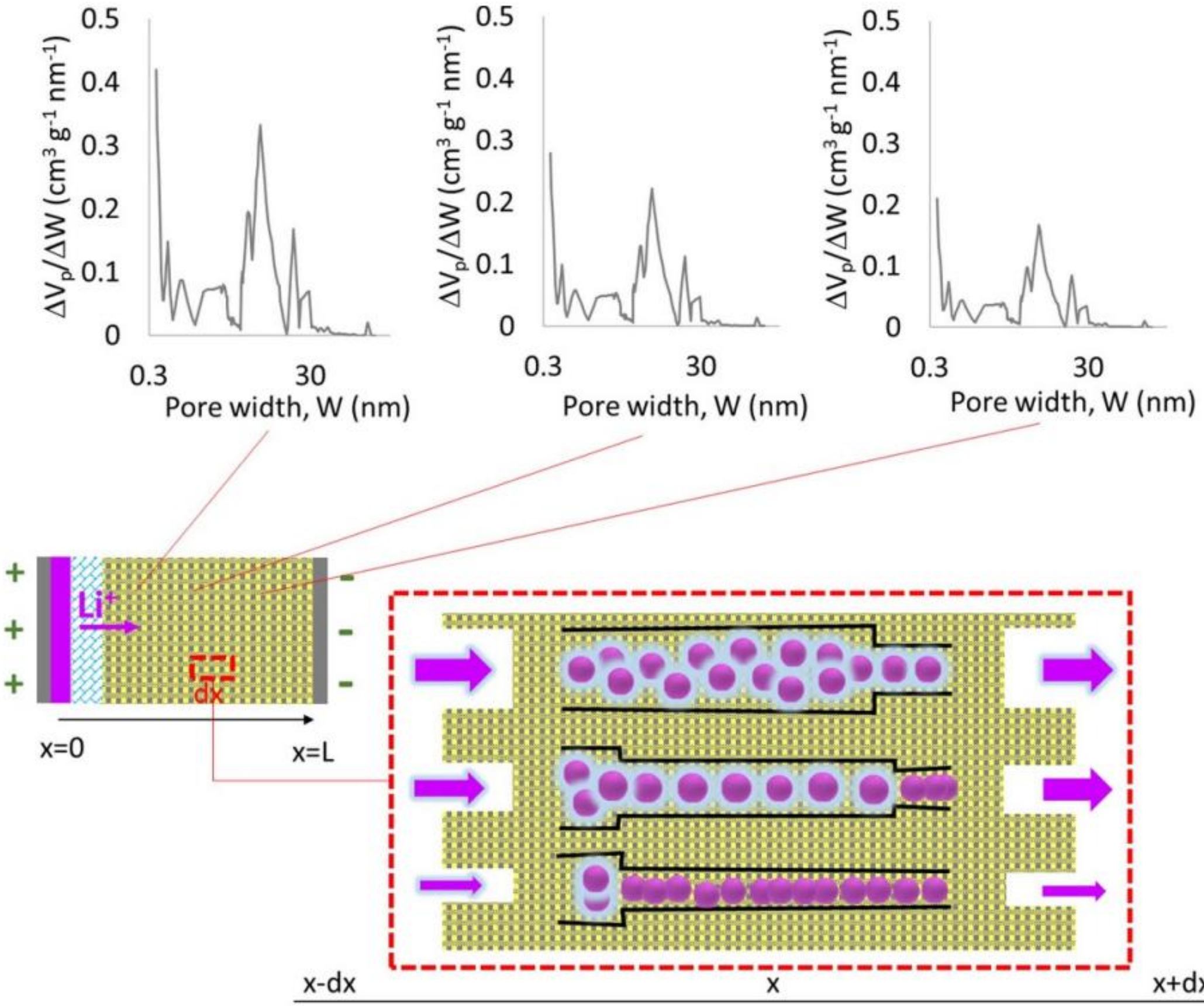

Figure 18. Diagram of continuum volume-averaged model for an electrochemical cell including anode, separator and cathode,

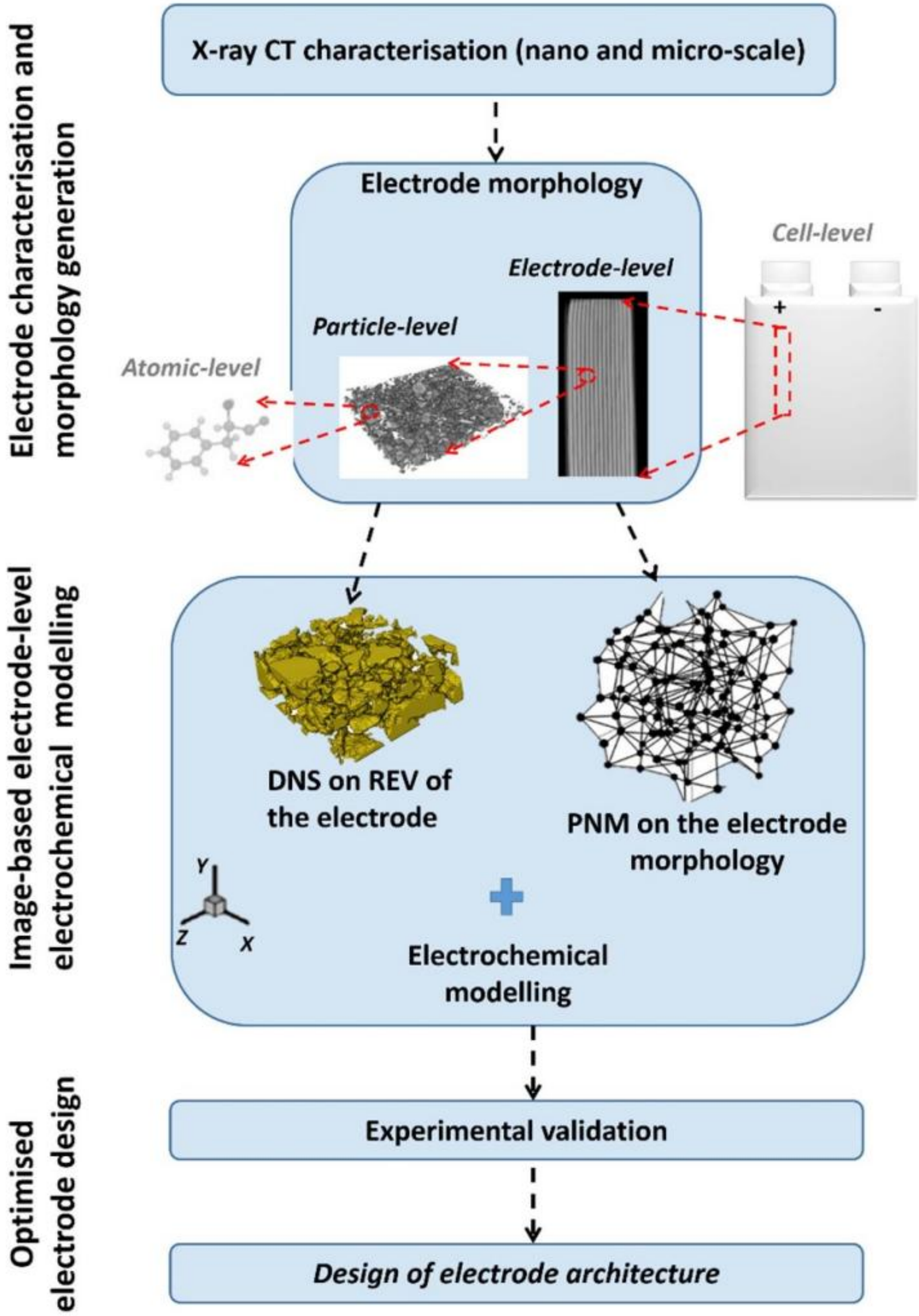

Figure 20. Roadmap of electrode-level modelling of LiS batteries to optimise electrode design, characteristics and architecture. This approach would include generation of electrode morphology using x-ray CT characterisations, combined use of electrochemical modelling with particle-level DNS models and an electrode-level PNM model to evaluate the effect of

Figure 7. Comparison of the critical metric solid electrolyte volume/capacity E/C ratio to the thickness of polymer, oxide, and sulfide solid electrolytes, extracted from data reported by Sun *et al* [51]. The shaded area represents the critical region of $<5\ \mu l\ mA\ h^{-1}$.

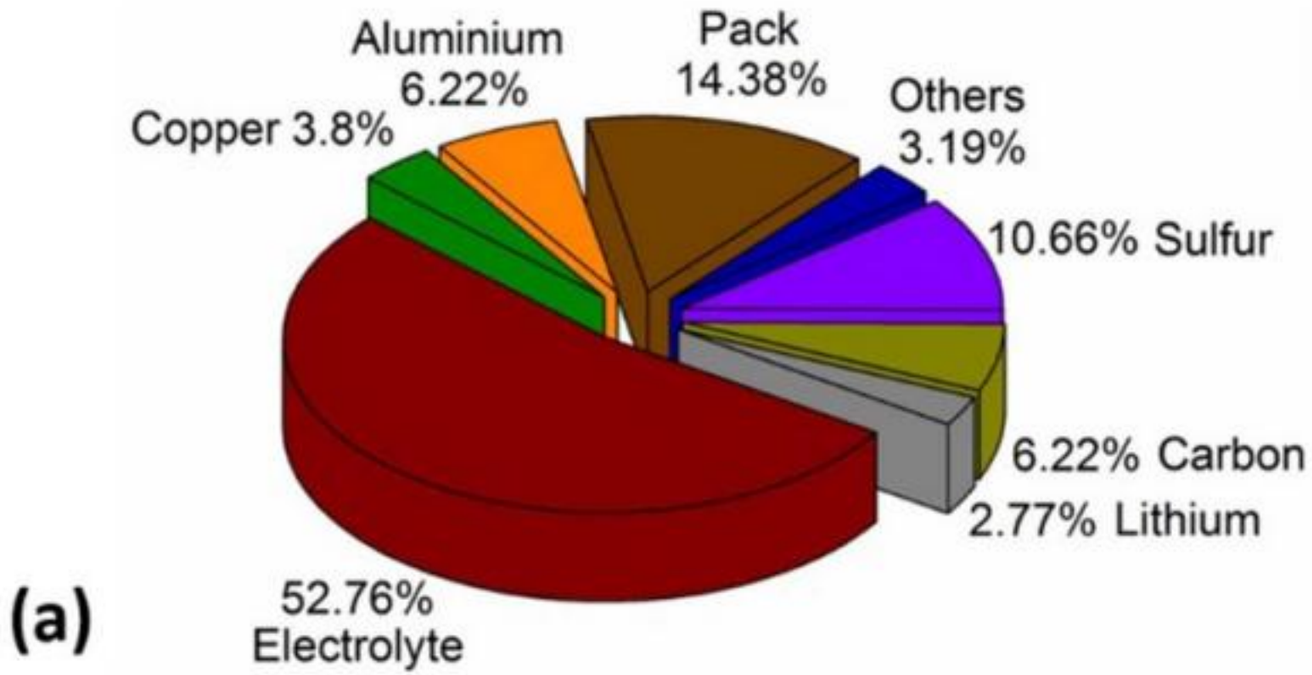

Others	
Material	**Ratio (%)**
Separator	1.87
Binder	0.89
Tab	0.42

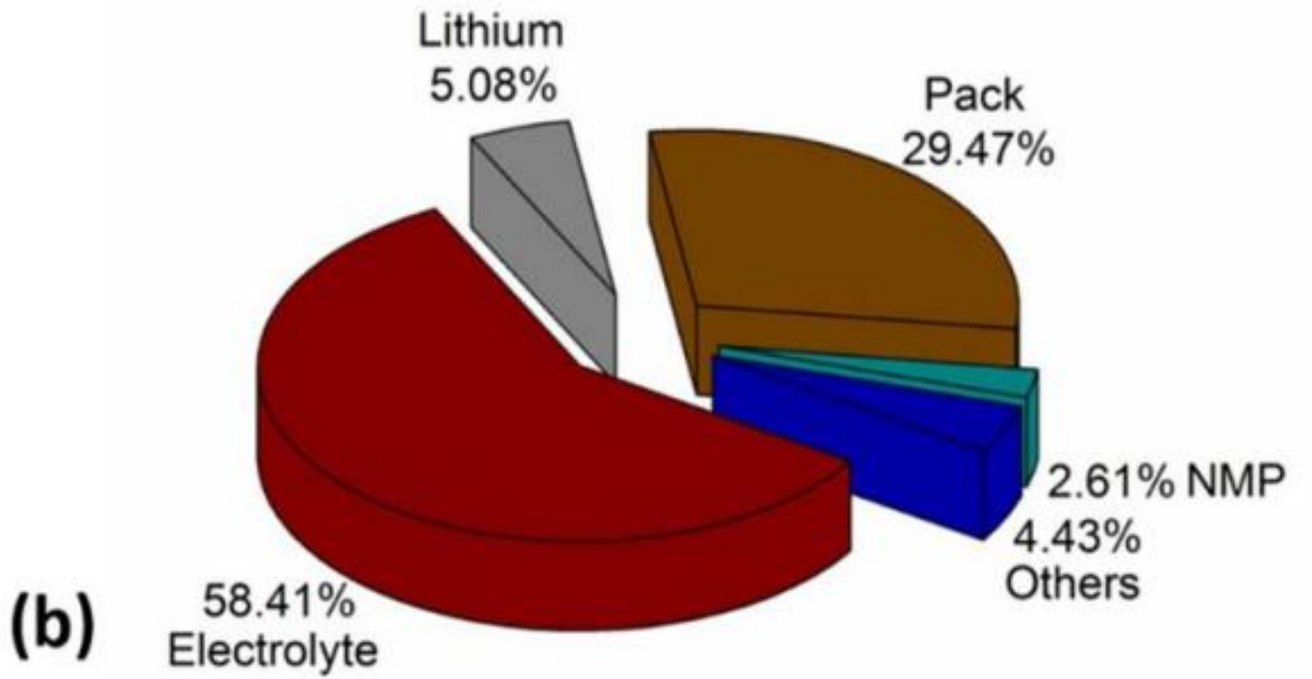

Others	
Material	**Ratio (%)**
Separator	1.47
Tab	1.16
Copper	0.91
Aluminium	0.41
Carbon	0.34
Binder	0.11
Sulfur	0.03

Figure 28. Typical (a) weight and (b) cost constituents of a Li–S pouch cell, illustrating areas in which cost reduction may be obtained. Adapted using data extracted from Yang *et al* [7].

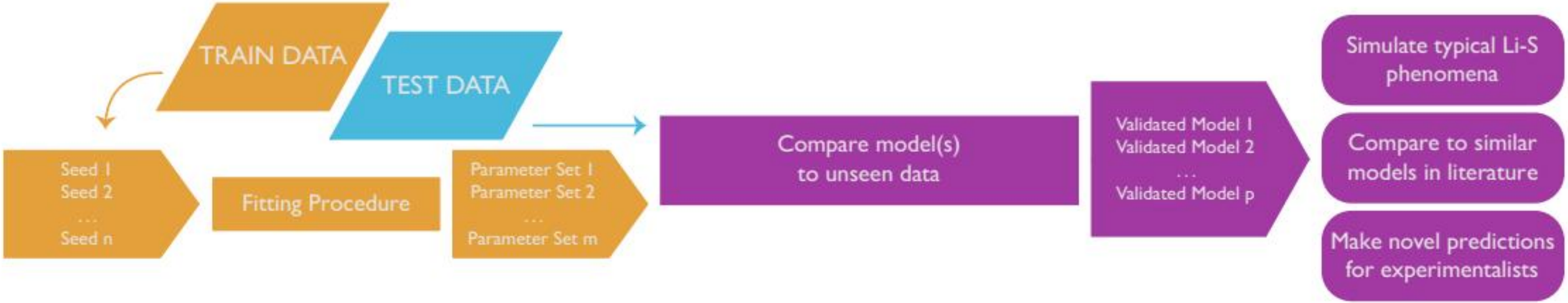

Figure 21. Model validation workflow showing the separation of empirical data into separate test and train sets. A number $n > 1$ of initial seeds to the fitting procedure are given, producing a number $m < n$ viable parameter sets. Each parameter set is then used to simulate the experiments performed to produce the test data. From the m parameter sets, a number $p < m$ will accurately model the unseen data. Each of the p parameter sets yields p models that have been appropriately validated. These models can be

MTSL

C50

0.3 ms
1.3 ms
2.3 ms
3.3 ms
4.3 ms
5.3 ms

13.1 Å

W49

4
5
7
6
^{19}F

0.3 ms
1.3 ms
2.3 ms
3.3 ms
4.3 ms
5.3 ms

-46.5 -46.6 -46.7 -46.8 -46.9

^{19}F ppm

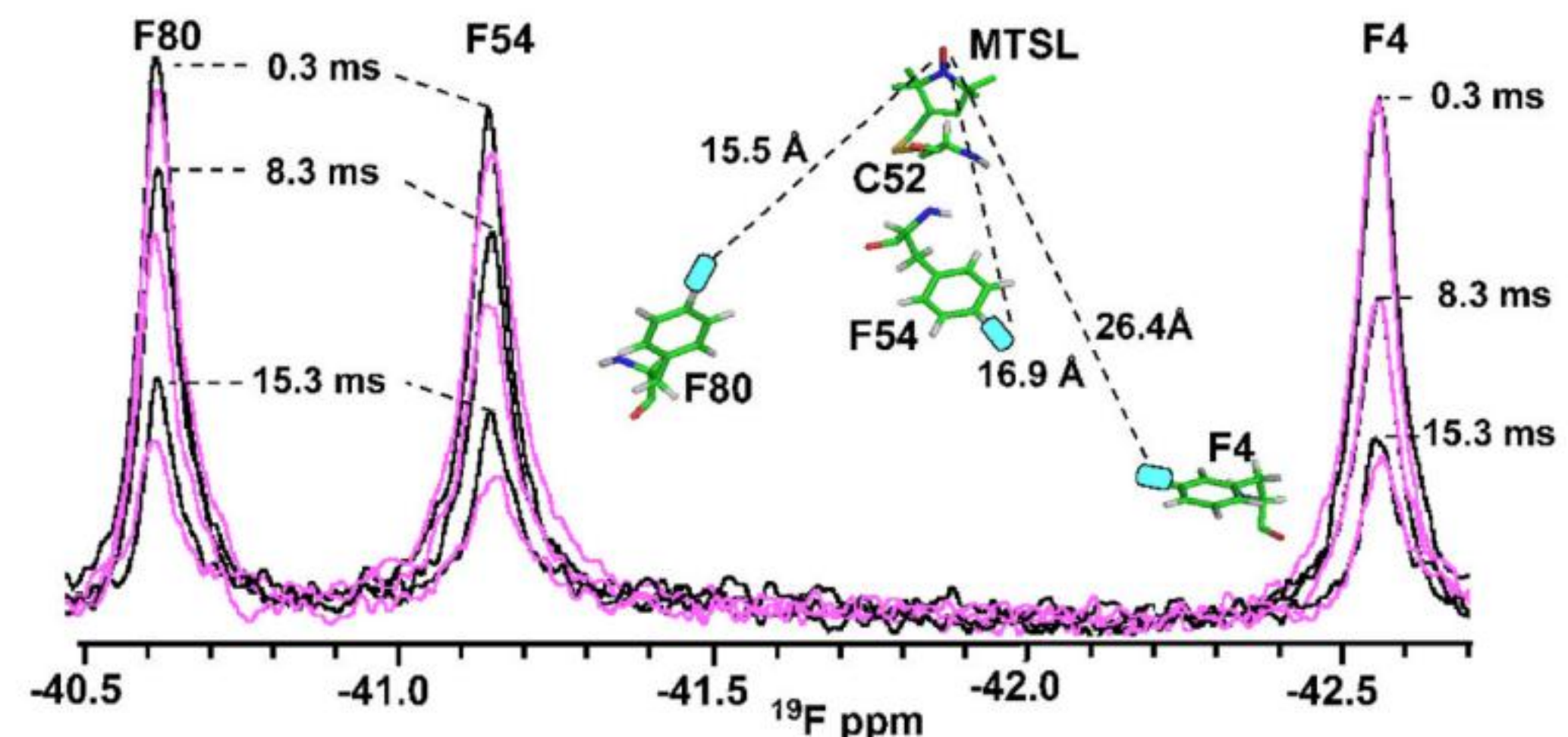
F80
F54
0.3 ms
8.3 ms
15.3 ms
MTSL
15.5 Å
C52
F54
26.4Å
16.9 Å
F80
F4
F4
0.3 ms
8.3 ms
15.3 ms
-40.5
-41.0
-41.5
-42.0
-42.5
19F ppm

A

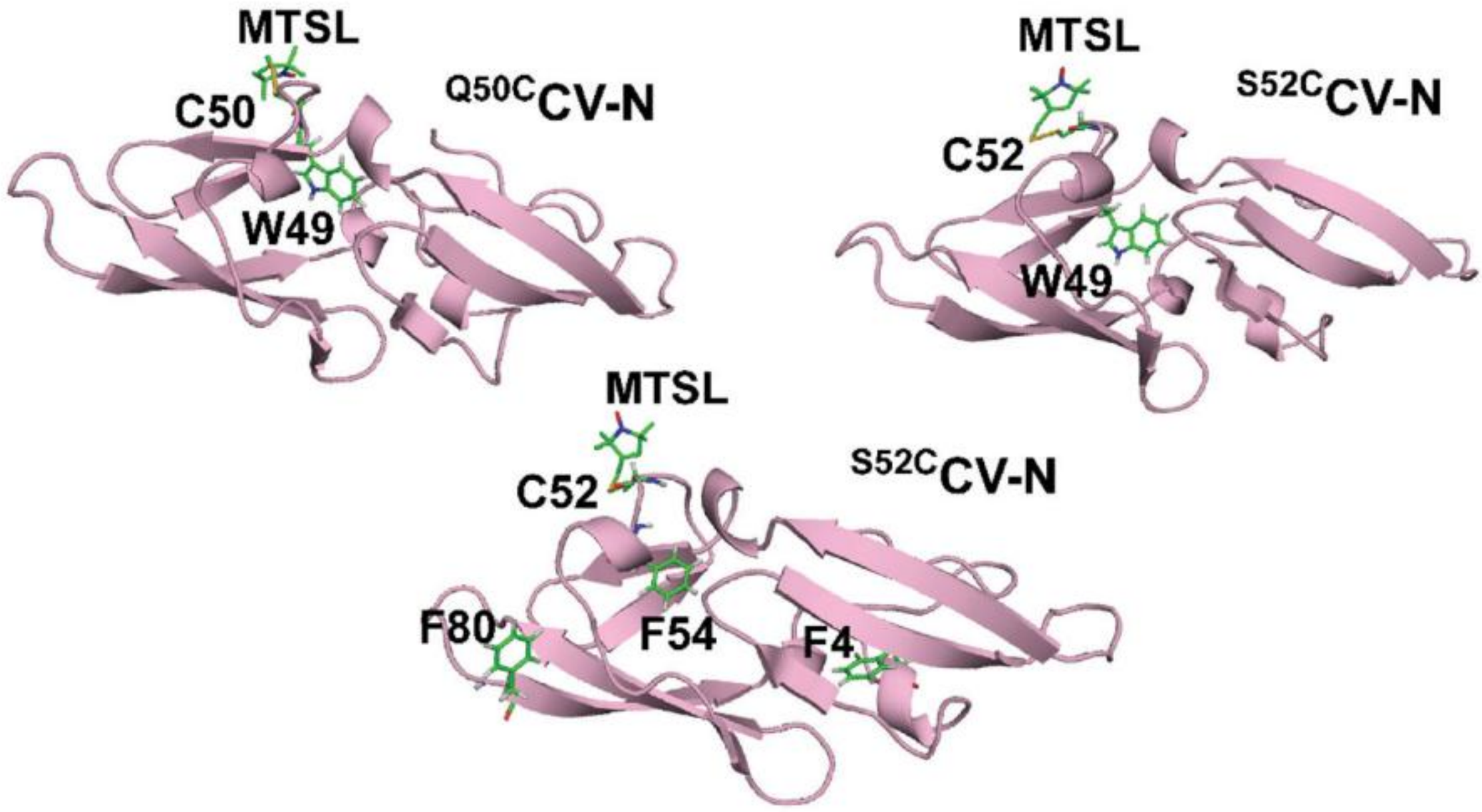
MTSL
C50
Q50CCV-N
W49
MTSL
C52
S52CCV-N
W49
MTSL
C52
S52CCV-N
F80
F54
F4

B

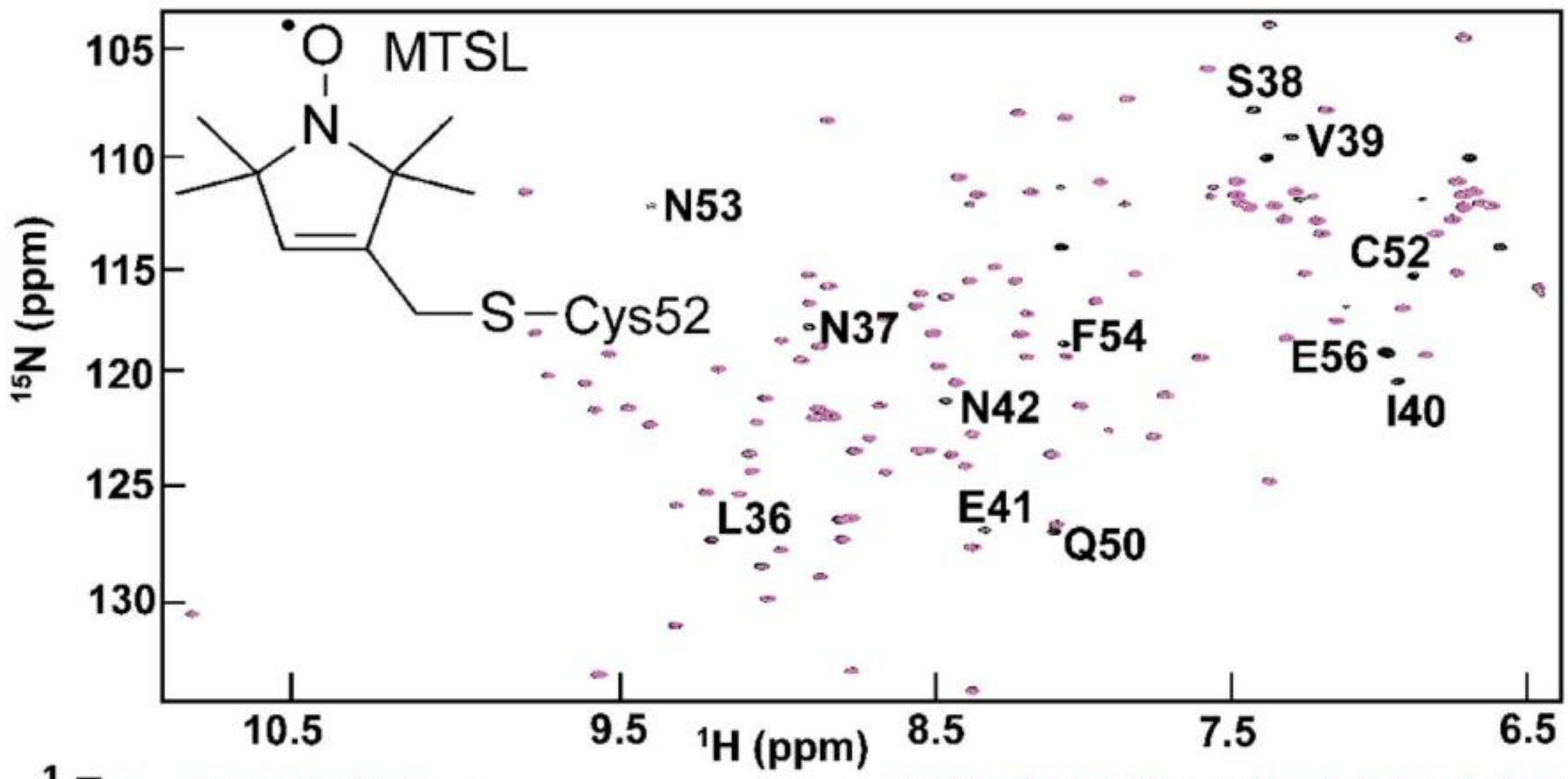
MTSL
S–Cys52
15N (ppm)
105
110
115
120
125
130
10.5
9.5
1H (ppm)
8.5
7.5
6.5
S38
V39
C52
E56
I40
N53
N37
F54
N42
L36
E41
Q50

C

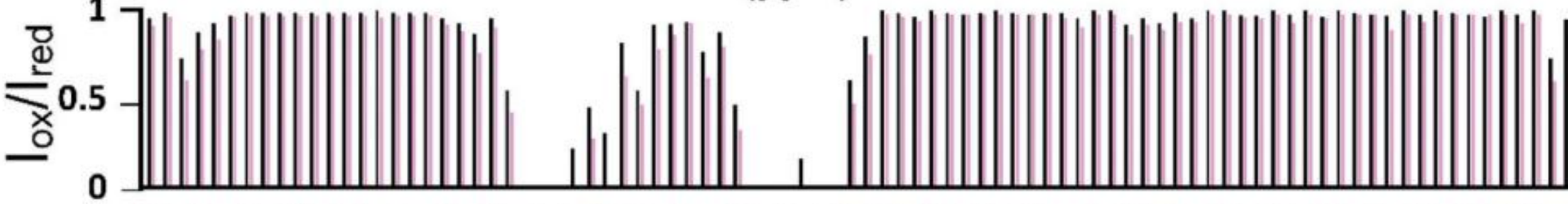
Iox/Ired
1
0.5
0
14 17 20 23 26 29 32 35 38 41 44 47 50 53 56 59 62 65 68 71 74 77 80 83 86 89 92 95 98

D

Distance (Å)
25
20
15
10
5
0
14 17 20 23 26 29 32 35 38 41 44 47 50 53 56 59 62 65 68 71 74 77 80 83 86 89 92 95 981
Residue #

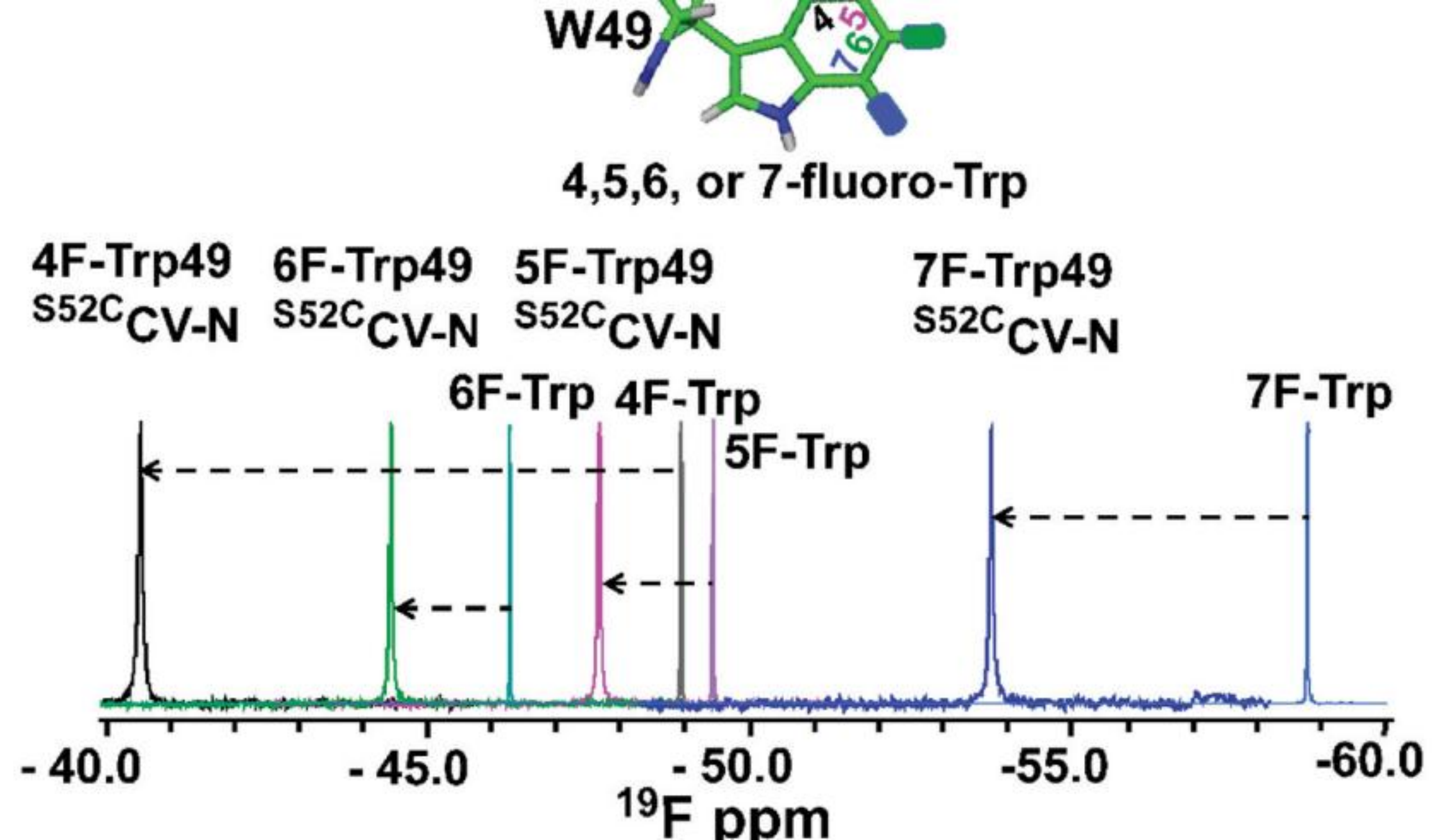
W49
4
5
6
7
4,5,6, or 7-fluoro-Trp
4F-Trp49
S52C CV-N
6F-Trp49
S52C CV-N
5F-Trp49
S52C CV-N
7F-Trp49
S52C CV-N
6F-Trp
4F-Trp
5F-Trp
7F-Trp
- 40.0
- 45.0
- 50.0
-55.0
-60.0
19F ppm

DEPARTMENT OF HEALTH & HUMAN SERVICES · USA

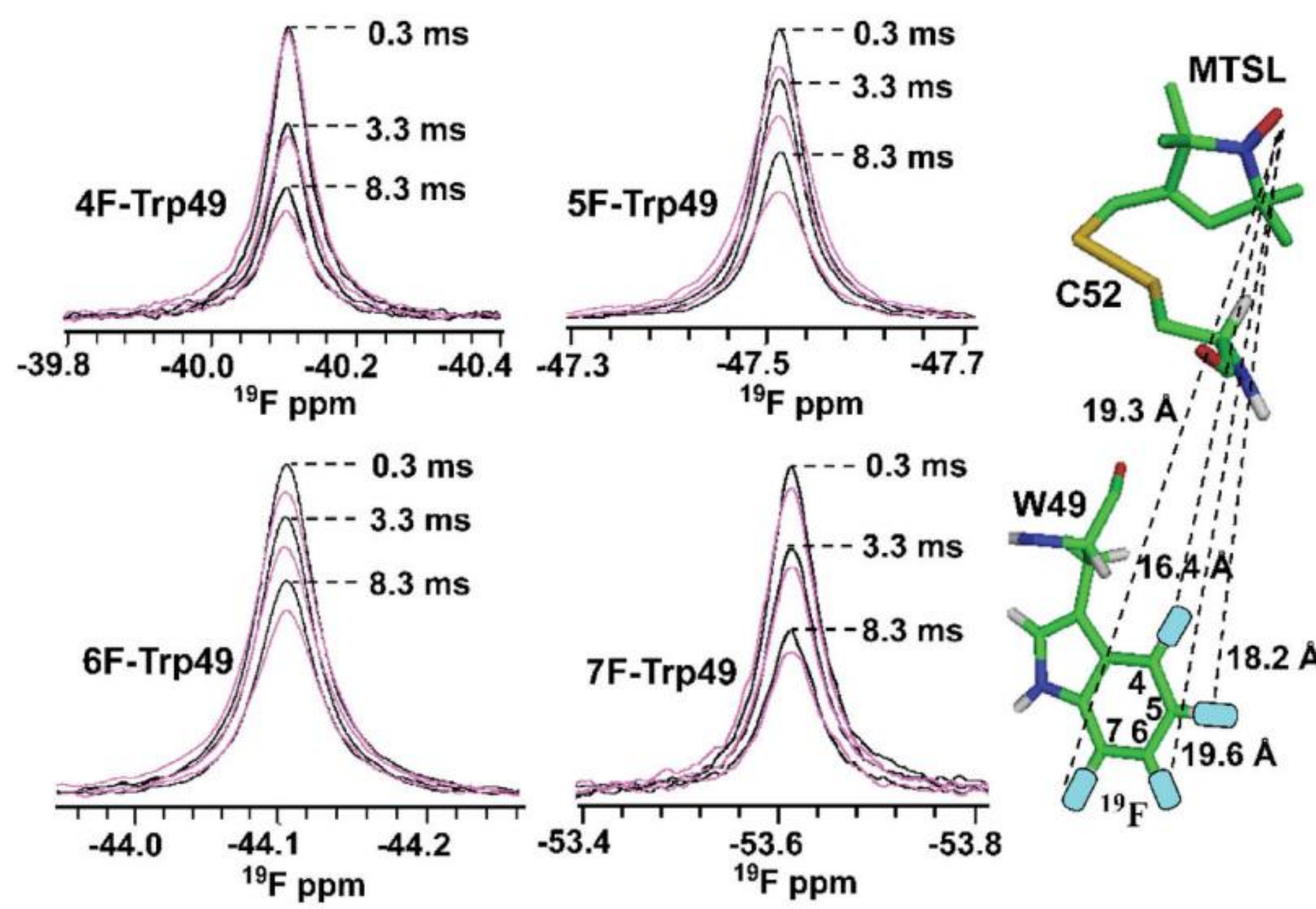
0.3 ms
3.3 ms
8.3 ms
4F-Trp49
-39.8
-40.0
-40.2
-40.4
19F ppm
0.3 ms
3.3 ms
8.3 ms
5F-Trp49
-47.3
-47.5
-47.7
19F ppm
MTSL
C52
19.3 Å
0.3 ms
3.3 ms
8.3 ms
6F-Trp49
-44.0
-44.1
-44.2
19F ppm
0.3 ms
3.3 ms
8.3 ms
7F-Trp49
-53.4
-53.6
-53.8
19F ppm
W49
16.4 Å
18.2 Å
19.6 Å
4
5
7
6
19F